Machine learning (ML)-based mineral prospectivity mapping (MPM): Detecting Iranian plateau high-potential metallogenic zones using geospatial big data

Vahid Teknik
vahid.teknik@gmail.com

Iman Monsef
Amr Abdelnasser
Abdolreza Ghods

Research Article

Keywords: Geospatial Big Data, Machine Learning, Mineral Prospectivity Mapping, Artificial Intelligence, Green exploration, Ore Deposits, Iran

Posted Date: September 30th, 2025

DOI: https://doi.org/10.21203/rs.3.rs-7730637/v1

Additional Declarations: The authors declare no competing interests.

Abstract

Recent advances in Artificial Intelligence (AI) and Machine Learning (ML) methods have significantly enhanced Mineral Prospectivity Mapping (MPM). These AI-based algorithms offer high capability for regional-scale mapping of underexplored ore deposits. However, there are still significant methodological challenges, particularly in integrating multidimensional, heterogeneous geospatial datasets and handling their inconsistencies with sparse and spatially clustered distributed known mineral ore deposits. The current study presents a novel framework to address these challenges. We developed a training dataset comprising 69 training features derived from geological, geophysical, and lithospheric raster grids. Vector-based geological features were systematically converted into raster grids, where each pixel encodes the minimum distance to the nearest structural and lithological boundaries. Therefore, one can capture the influence of structural and lithological proximity on metallogenic zones. The training target is generated by combining the spatial distribution of seven major metallic ore deposits and converting their spatial locations into a continuous raster grid of spatial density of metallic ore occurrence. Seven ML algorithms with their 24 subtypes are used to predict the spatial density of mineral deposits. Among them, the Ensemble Bagged Trees method showed optimum prediction performance by achieving the lowest Root Mean Square Error (RMSE) and the highest coefficient of determination (R^2). The optimized model was applied to calculate a predictive MPM across the Iranian plateau. To pinpoint underexplored high-potential zones, residual spatial density anomalies were calculated by subtracting the observed ore occurrence spatial densities from the predicted prospective grid. The residual spatial density anomalies reveal several promising areas, such as the Malayer-Isfahan Pb-Zn zone along the Zagros suture zone. The residual anomalies show significant potential extended southward of the KaraDagh copper zone in NW Iran. The results also indicate high potential zones in central and eastern Iran, notably near the Bafgh, Nehbandan-Ferdous, and Jiroft-Shahrebabak metallogenic zones. Regional-scale AI-aided regression analysis enhances our understanding of ore deposit distribution across the Iranian plateau. This insight provides a strategic foundation for future national-scale exploration programs by improving efficiency, reducing risk and cost, and narrowing the area of detailed exploration.

Highlights

- An AI-aided approach was developed for mineral prospectivity mapping.
- Sixty-nine geological and geophysical variables were used for model training.
- The predicted spatial density of ore deposits was estimated across the Iranian plateau.
- Residual spatial density anomalies highlight high-potential underexplored ore deposit zones.
- The study offers actionable insights for reducing future exploration risks and costs.

1. Introduction

The increasing global demand for new metallic ore resources is accompanied by declining discoveries in recent decades, since deposits with surface outcrops have mostly been discovered. It is speculated that unexplored deposits are either concealed beneath sediment cover or obscured by complex tectono-magmatic events (Davies et al., 2021). Traditional exploration methods such as geological, geochemical, and geophysical surveying, and drilling are used to identify hidden resources (Zhao, 2007; Dentith and Mudge, 2014; Adiri et al., 2020; Dentith et al., 2020). However, the traditional methods are often expensive and time-consuming and face challenges in handling diverse big data formats with typically low resolution and inadequate survey coverage, particularly at the regional scale (Gonzalez-Alvarez et al., 2020).

To address these challenges and limitations, Mineral Prospectivity Mapping (MPM) has emerged as a fast, cost-effective, and data-driven approach for prioritizing potential metallogenic zones. The MPM approach leverages different geospatial data and insights from known deposits to predict new exploration targets on a regional scale. Formation of ore deposits is governed by various complex geological processes including magmatic differentiation, hydrothermal fluid circulation, sediment accumulation, metamorphic transformation, and supergene enrichment (Bierlein et al., 2006; Groves and Bierlein, 2007; Kesler and Simon, 2015). Despite substantial progress in understanding these processes, integration of diverse geospatial datasets into a comprehensive mineral exploration model remains challenging (McCuaig et al., 2010).

The recently introduced artificial intelligence (AI) and machine learning (ML) algorithms have revolutionized geoscientific big data analysis (Bergen et al., 2019; Lösing and Ebbing, 2021; Woodhead and Landry, 2021; Guo and Yang, 2023; Li et al., 2023; Chukwu et al., 2024; Teknik, 2024). Recent innovative AI advances are also revolutionizing mineral prospectivity modelling by enhancing processing ability, improving targeting accuracy, and optimizing exploration strategies while minimizing environmental impacts. AI-based methods have been successfully used for uncovering complex relationships between known mineral deposits and associated geological and geophysical datasets (Chen and Wu, 2017; Maepa et al., 2021; Parsa and Carranza, 2021; Parsa and Maghsoudi, 2021; N. Yang et al., 2022; Yin et al., 2023; Zuo and Xu, 2023; Li et al., 2024; Wake et al., 2024). ML-based MPM workflow employs statistical models to predict mineral potential by analyzing key attributes such as lithology, structural patterns, and geophysical anomalies. Then the trained ML models could be used to predict the likelihood of mineral deposits in less explored regions (Holden et al., 2008; Carranza and Laborte, 2015; Xiong and Zuo, 2018; McMillan et al., 2021; Benaissi et al., 2022). However, the challenges remain because of the scarcity of well-known deposits, their irregular distributions, as well as the complexity of ore formation, which complicate the development of universal models for different ore deposits (e.g., Xiong et al., 2018).

In this study, we apply AI-based techniques to address the regional-scale exploration challenges on the Iranian plateau. Our approach investigates the statistical relationship between the spatial density of metallic deposits with geological and geophysical data. An integrated metallic mineral dataset was formed by compiling seven ore deposits of iron (Fe), copper (Cu), lead (Pb), zinc (Zn), gold (Au), silver (Ag), and magnesium (Mg). The spatial density of mineral deposits served as a target variable within a series of regression-based learning models, aiming to detect spatial patterns related to metallogenic potential. A novel transformation of complex vector-based geological maps into raster grid formats was introduced in this study to facilitate their integration into a geospatial big data framework suitable for machine learning analysis. We introduced an adaptive AI-aided workflow for regional-scale mineral prospectivity mapping that systematically evaluates the predictive performance of multiple regression algorithms to optimize the detection of the prospective zones across the Iranian plateau. The proposed methodology overcomes the heterogeneity and inconsistency of datasets and provides valuable guidance for prioritizing underexplored metallogenic zones. The approach provides a cost-effective solution with reduced financial risks, thereby facilitating more efficient and targeted mineral resource exploration efforts with minimum environmental impacts.

2. Geological framework of the Iranian plateau

The Iranian plateau represents a complex and dynamic geological setting, where shaped by a series of temporally and spatially diverse geodynamic and tectonic events. Its evolution is closely linked to the sequential opening and closure of the Paleo- and Neo-Tethyan oceans, events that played a crucial role in the region's tectonostratigraphic architecture and metallogenic development (Stampfli and Borel, 2002). Therefore, Iranian plateau is composed of continental blocks that are separated by Tethyan oceanic suture zones. The convergence between Arabian and Eurasian plates, accompanied by the progressive accretion of multiple continental microplates along the southern margin of Eurasia, where it has fundamentally shaped the present-day configuration of the Iranian plateau (Stocklin, 1968; Stöcklin, 1974; Berberian and King, 1981; Alavi, 1996). The ore deposits' formation, their types and spatial distribution are closely associated with the magmatic history across the Iranian plateau, especially where the various phases of crustal extensions and compressions within the Tethyan orogeny, extending from the Early Palaeozoic to the Cenozoic (Stampfli, 2000; Richards, 2015). Many of the major crustal-scale lineaments were reactivated during Mesozoic and Cenozoic tectonic events and facilitated both extensive crustal extension and exhumation intrusions (Shahabpour, 1999; Moritz et al., 2006; Meshkani et al., 2013; Bagheri, 2015).

The exposures of Neoproterozoic-Early Cambrian crystalline basement rocks in the Iranian plateau and the trend of magmatic belts provide key controls on the distribution and localization of mineral deposits (Meshkani et al., 2013). Extensional tectonics associated with the rifting of the Neo-Tethys ocean led to the detachment of the Cimmerian terranes from northern Gondwana during the Permian to Triassic. These Cimmerian terranes include the Anatolide-Tauride, Central Iran, Tibet, and Indochina. The northward drifting of these terranes ended with the event of their collision with the southern margin of Eurasia from the Late Triassic to the Early Jurassic, which led to the formation of the Paleo-Tethyan suture zone (Stampfli, 2000; Stampfli and Borel, 2002; Richards, 2015). During the Mesozoic and Cenozoic, the subduction of the Neo-Tethys ocean beneath the Central Iran blocks formed fore-arc basins, extensive magmatism, and back-arc basins throughout the Iranian plateau (e.g., Monsef et al., 2022).

One of the most significant magmatic arcs within the Iranian plateau is the Urumieh-Dokhtar magmatic arc (UDMA), which is marked by a subduction-related magmatism caused by the subduction of the Neo-Tethys ocean beneath the Central Iran block. The Urumieh-Dokhtar magmatic arc mostly formed by pronounced magmatic flare-ups throughout the Eocene to the Oligocene (ca. 55 – 25 Ma) (Verdel et al., 2011; Chiu et al., 2013). The magmatic flare-ups of UMDA were followed by widespread post-collisional extensional magmatism during the Neogene, which is attributed to the slab break-off or lithospheric delamination (e.g., Allen et al., 2013).

The composite tectonic unit of the Central Iranian block consists of three major blocks of Lut, Tabas, and Yazd (Fig. 1). Eastern Iran includes the Sistan suture zone and Lut block. Eastern Iran is characterized by intense Tertiary strike-slip faulting, widespread magmatism, and N-S trending ophiolitic belts (e.g., Omidianfar et al., 2020). Subduction-related magmatism associated with these tectonic processes has contributed significantly to the metallogenic evolution of Eastern Iran (Arjmandzadeh et al., 2011; Alaminia et al., 2013; Richards, 2015). In the northeast of Central Iran and north of Eastern Iran, the E-W trending Sabzevar magmatic-ophiolitic belt extends about 700 km along the northern side of the Dorouneh fault. This belt is bound to the Kopeh-Dagh zone (Eurasian plate) in its north. The Kopeh-Dagh Mountains mark the most northeastern edge of the deformation zone of the Arabia-Eurasia collisional zone in the Iranian plateau. The Kopeh-Dagh is marked with a ~ 10 km deep folded Mesozoic-Tertiary sediment sequence. The Sistan and Sabzevar ophiolites represent the evidence of Neo-Tethys back-arc basins and serve as an important lithological marker delineating the boundaries of major tectonic units (Stöcklin, 1968; Richards, 2015).

During the Neogene, the Arabian plate collided with the Central Iran block, leading to the formation of the Bitlis-Zagros suture zone (Stöcklin, 1968; Berberian and King, 1981; Boulin, 1991; Stampfli and Borel, 2002). The continuous northward convergence of the Arabian plate gave rise to the Zagros fold and thrust belt with an extensive NW-SE-trending orogenic belt in the south of the Zagros suture zone. The Zagros orogenic system remains tectonically active, particularly where the Main Recent Fault (MRF) and the Main Zagros Thrust (MZT) consume part of the regions' ongoing continental convergence (Stampfli and Borel, 2004; Richards, 2015; Berberian, 1995; Sepehr and Cosgrove, 2004) (Fig. 1). The Zagros suture zone lies approximately along MRF and MZT. The Zagros ophiolites are discontinuously exposed along the Zagros suture zone. The ophiolites can be divided into two parallel belts of the inner and outer Zagros ophiolitic belts. In the southwest periphery of the Central Iran block, the inner Zagros ophiolitic belt comprises Nain, Dehshir, and Baft ophiolites. The outer Zagros ophiolitic belt, along the Main Zagros Thrust, comprises Kurdistan, Kermanshah, Neyriz, and Hajiabad ophiolites (e.g., Monsef et al., 2018).

The southeastern continuation of the Zagros fold and thrust belt identifies the Makran accretionary prism that extends for ~ 900 km from southeastern Iran to southeastern Pakistan. In this region, the last piece of Arabian oceanic lithosphere is currently being subducted beneath the Makran accretionary complex in the south of Iran and Pakistan. The Makran subduction zone, which exhibits an anomalously low level of magmatism, is associated with the development of the Cenozoic Jazmurian Basin, interpreted as an old back-arc basin (Glennie et al., 1990; Shahabpour, 2010; Penney et al., 2017; Burg, 2018; Teknik et al., 2024). The Jazmurian basin is covered with a thick sedimentary cover reaching its maximum thickness of ~ 20 km in its eastern edge (Enayat and Ghods, 2023; Mehrdar et al., 2025). The Zagros ophiolites continue southeast, toward the Makran ophiolites. The Makran ophiolites can also be divided into two distinct belts, consisting of the inner and outer Makran ophiolitic belts (e.g., Monsef et al., 2019).

3. Ore deposits of the Iranian plateau

Different world-class ore deposits occurred in the Iranian plateau, making the Iranian plateau one of the most important metallogenic zones in western Asia and central Tethys (Fig. 2 and Table 1). The most prominent ore deposits on the Iranian plateau are iron (Fe), copper (Cu), lead-zinc (Pb-Zn), and gold (Au) deposits. This is indebted to the complex geologic setting of the plateau, manifested by a series of tectonic, magmatic, hydrothermal, and metamorphic events along the major active geological boundaries. These processes have facilitated the formation of distinct metallogenic zones. Each zone is particularly associated with the distinct tectonic structures such as faults, shear zones, and suture boundaries, as well as geodynamic events such as subduction, continental collision, and post-collisional extension. The investigation of ore deposits was done using various methods such as remote sensing, geochemical analyses, and structural surveys (e.g., Zarasvandi et al., 2005; Golmohammadi et al., 2015; TaleFazel et al., 2019).

The influence of the geodynamic processes on the genesis of the Iranian ore deposits is addressed by comprehensive geological studies. In this context, the evolution of Tethyan oceans and associated tectono-magmatic activities caused the distribution of ore deposits within the Iranian plateau. Indeed, the sequential divergent and convergent events of the Tethyan oceans provide a suitable geological framework for the formation of a variety of ore deposits (e.g., porphyry, skarn, epithermal, MVT, VMS, and SEDEX). Igneous rocks, including volcanic, sub-volcanic, and plutonic bodies, crystallized from the magmas that derived from the partial melting of the upper mantle and then differentiated in crustal magma chambers. The metalliferous hydrothermal fluids exsolved from the evolved melts caused Fe, Cu, Pb-Zn, and Au mineralisation in the form of massive ores, breccias, veins, and veinlets at the shallow levels.

The subduction of Tethyan oceans beneath the Iranian continental fragments produced arc-related and extensional back-arc basin magmatism with mostly calc-alkaline to alkaline affinities. After the collision between the Arabia and Central Iran or Lut and Afghan blocks, the lithospheric delamination and subsequent asthenospheric upwelling led to decompression melting of previously metasomatized sub-continental lithospheric mantle and the generation of high-K alkaline to shoshonitic volcanism and plutonic bodies. Porphyry deposits in Iran are intrusion-related deposits that are products of magmatic-hydrothermal activity at shallow crustal levels in subduction and post-collisional tectonic settings. Primarily copper, but also molybdenum and gold occur closely related to epizonal intrusions of porphyric magmatic rocks (e.g., Zarasvandi et al., 2005, 2019; Hezarkhani, 2006; Aghazadeh et al., 2015). Skarn-type deposits in Iran are formed by metasomatic replacement of carbonate rocks by hydrothermal fluids derived from granitoid bodies in subduction and collisional tectonic settings. They are characterized by the presence of copper and iron (e.g., Golmohammadi et al., 2015; Hassanpour and Rajabpour, 2020). Epithermal deposits in Iran, ranging from high-sulfidation to low-sulfidation types, are connected with terrestrial volcanism that formed by near-surface magmatic-hydrothermal processes circulating through fault systems and veins. They are often hosted within volcanic and volcaniclastic rocks remarkable as a major source of gold, silver, copper, lead, and zinc (e.g., Mehrabi et al., 2016; TaleFazel et al., 2019). Mississippi Valley-type (MVT) deposits in Iran are a type of epigenetic carbonate-hosted sulfide ore deposit, primarily known for their lead and zinc mineralization. These deposits are characterized by their migration of ore-forming fluids within fault and karst systems in a collisional tectonic setting (e.g., Rajabi et al., 2013; Qaderi et al., 2024). Volcanogenic massive sulphide (VMS) deposits in Iran are formed by submarine volcanic activity, or more precisely, seafloor hydrothermal activity related to the arc/intra-arc rifts and back-arc basins. The most important metals in VMS are copper, lead, and zinc, with trace contents of gold and silver that are hosted in volcano-sedimentary succession (e.g., Hajsadeghi et al., 2018; Mousivand et al., 2018). Sedimentary exhalative (SEDEX) deposits in Iran are very similar in genesis to the VMS deposits that are primarily known for containing often lead and zinc with subordinate silver and iron formed by the precipitation of metal sulfides from hydrothermal fluids onto the seafloor sediments of arc/intra-arc rifts and back-arc basins (e.g., Maghfouri and Hosseinzadeh, 2018; Maghfouri et al., 2025). Accordingly, these deposits within the Iranian plateau are formed in an integral ore-forming system and have a genetic link with magmatic-hydrothermal processes. These magmatic-hydrothermal activities have a relationship to the evolution of the Tethyan oceans.

Central Iran, particularly the Bafgh region, is recognized as one of the most metallogenically significant zones in the Tethys belt, especially for its exceptional concentration of iron ore deposits. The region hosts some of the largest iron ore bodies within the Iranian plateau, such as the Choghart and Sechahoon deposits. These gigantic deposits are primarily associated with Neoproterozoic metamorphic and igneous complexes (Ghorbani, 2013a; Korehie et al., 2019). High aeromagnetic anomalies around the Bafgh region imply a high potential for further iron metallogenic zones (e.g., Torab and Lehmann, 2007). Iron ore spatial distribution extends beyond Central Iran into the Sanandaj-Sirjan zone, Eastern Iran, and the Urumieh-Dokhtar magmatic arc. It includes a variety of deposit types such as magmatic, skarn, volcanogenic, and sedimentary types (e.g., Stosch et al., 2011; Nabatian et al., 2015; Hassanlouei and Rajabzadeh, 2019).

Numerous porphyry and skarn-type cupper ore deposits are predominantly associated with the Urumieh-Dokhtar magmatic arc. Significant clusters of porphyry copper deposits are found in the Jiroft-Shahrebabak zone (Fig. 2d), where the world-known porphyry copper deposits of Sarcheshmeh and Meiduk have been discovered (Fig. 2a). A similar tectonomagmatic activity and emplacement of magmatic intrusions along Urumieh-Dokhtar magmatic arc formed the Mazraeh and Sungon copper deposits (Fig. 2a), together with a cluster of minor deposits along the KaraDagh zone in northwestern Iran (Zarasvandi et al., 2007; Hezarkhani, 2008; Mollai et al., 2009; Asadi et al., 2014; Kheyrollahi et al., 2018).

Lead-zinc deposits are widespread across the Sanandaj-Sirjan zone and more specifically the Malayer-Isfahan zone. Other major lead-zinc metallogenic zones are situated in Central Iran and the Alborz regions (Ghorbani, 2013b). Considering the diverse tectono-magmatic and metamorphic events, the various metallic ore deposits have been categorized based on their spatial distributions and types (Ghorbani, 2013b).

The gold deposits on the Iranian plateau are relatively less explored. However, the distribution of gold deposits is primarily extended within the Sanandaj-Sirjan metamorphic zone as well as along the Urumieh-Dokhtar magmatic arc, Azerbaijan-Alborz, and Eastern Iranian magmatic belts. These regions host epithermal, porphyry-related, and orogenic deposit types, reflecting the complex geodynamic evolution of the Tethyan metallogenic belt across the Iranian plateau (e.g., Moritz et al., 2006; Richards et al., 2006; Daliran, 2008; Geranian et al., 2016). The silver deposits, similar to gold deposits, are typically connected to the copper metallogenic zones. The spatial distribution of the magnesium mostly follows the trends of the Sistan suture zones (Fig. 2a).

In this study, the metallogenic zones delineated by Ghorbani (2013a) have been refined and updated by calculating the spatial density of mineral deposits (Fig. 2d). Regions exhibiting high spatial density (> 0.2 num/sq km) of mineral deposits have been identified. Consequently, the major metallogenic zones on the Iranian plateau are: (1) KaraDagh; (2) Takab-Tarom-Hashtjin; (3) Malayer-Isfahan; (4) Kashan-Natanz; (5) Toroud; (6) Anarak; (7) QaleBala; (8) Bafgh; (9) Khaf; (10) Nehbandan-Ferdous; (11) Jiroft-Shahrebabak; and (12) Kahnuj-Fanuj.

Table 1
List of major known Cu, Fe, Au, and Pb-Zn ore deposits throughout the Iranian plateau (after Meshkani et al., 2013 and references therein). The selected deposits here are grouped for qualitative evaluation of the AI-based models. Abbreviations: MVT, Mississippi Valley type deposit; VMS, Volcanogenic massive sulphide deposit; SEDEX, Sedimentary exhalative deposit.

Deposits	Long	Lat	Host/country rocks	Stratigraphic age	Major Commodity	Other accessory minerals	Genetic type	Tonnage and grade
Masjed daghi	46.936	38.875	Granite and andesitic rocks	Oligo-Miocene	Cu	Au	Porphyry	10 Mt – 0.7% Cu, 0.5 g/t Au
Mazraeh	46.983	38.625	Volcano-sedimentary rocks, granite, and limestone	Oligo-Miocene	Cu	Pb, Zn, Au, Ag	Skarn	1 Mt – 1.7% Cu, 0.3 g/t Au
Sungon	46.717	38.700	Monzodiorite and volcano-sedimentary rocks	Oligo-Miocene	Cu	Mo, Pb, Zn, Au, Ag	Porphyritic-skarn	290 Mt – 0.76% Cu, 0.015% Mo
Enjerd	46.933	38.683	Andesite, granite, and limestone	Cretaceous, Oligo-Miocene	Cu	Au, Fe	Skarn	300Mt – 0.85% Cu
Astamal	46.375	38.567	Andesite and tuff	Oligo-Miocene	Cu	Mo, Pb, Zn	Vein	> 1 Mt
Jarou	50.550	35.708	Andesite and andesitic basalt	Eocene-Oligocene	Cu	Pb, Zn	Vein	> 1 Mt
Veshnaveh	50.983	34.233	Andesitic basalt and tuff	Eocene	Cu		Vein	> 1 Mt
Deh madan	51.083	31.600	Limestone, dolomite, and sandstone	Cambrian	Cu	Zn, Pb, Co	MVT	> 1 Mt
Meskani	53.450	33.325	Trachyandesite and basalt	Eocene	Cu	Ni, Co, U, Bi, Au, Pb, Zn, Ag	Hydrothermal (volcanogenic)	~ 1 Mt.-2%Cu, 002% Ni, 15 g/t Ag
Talmesi	53.450	33.383	Trachyandesite and basalt	Eocene	Cu	Ni, Co, U, Bi, Au, Pb, Zn, Ag	Hydrothermal (volcanogenic)	~ 1 Mt – 2.2% Cu, 002% Ni
Ali abad	48.983	36.508	Porphyritic granodiorite and tuff	Oligo-Miocene	Cu	Mo	Porphyry	40 Mt – 0.7% Cu, 0.005% Mo
Darreh zereshk	53.842	31.567	Granodiorite, andesitic tuff and limestone	Eocene-Miocene	Cu		Porphyry	23 Mt – 0.68% Cu, 0.01% Mo
Chah mousa	54.867	35.475	Andesitic tuff and lava	Paleogene	Cu		Vein	> 1 Mt
Taknar	57.783	35.367	Rhyolite and schist	Late Paleozoic	Cu	Ag, Au, Pb, Zn	SEDEX	> 2 Mt – 3% Cu, 1.5% Zn, 1.%Pb

Deposits	Long	Lat	Host/country rocks	Stratigraphic age	Major Commodity	Other accessory minerals	Genetic type	Tonnage and grade
Qaleh zari	58.955	32.362	Andesitic to basaltic lava and tuff	Eocene	Cu	Fe, Au, Ag, Pb, Zn	Hydrothermal	1.3 Mt – 3% Cu, 2 g/t Au, 30 g/t Ag
Meiduk	55.200	30.467	Andesitic basalt and pyroclastic rocks	Miocene	Cu		Porphyry	500 Mt – 0.83% Cu, 0.01% Mo
Darreh-zerreshk	55.917	29.883	Volcano-sedimentary rocks and porphyritic diorite	Miocene	Cu	Mo, Pb, Zn	Porphyry	> 1 Mt 0.64%, 0.004% Mo
Sarcheshmeh	55.867	29.950	Porphyritic granodiorite and andesite	Eocene-Miocene	Cu	Mo, Au	Porphyry	1200 Mt – 0.7% Cu, 0.03% Mo, 0.08 g/t Au, 3 g/t Ag
Chahar gonbad	56.183	29.592	Porphyritic quartz diorite and andesitic tuff	Eocene-Oligo-Miocene	Cu	Pb, Zn, Au, Ag	Hydrothermal	3 Mt – 1.67% Cu
Sheikh aali	56.758	28.133	Pillow lava and volcanic rocks	Upper Cretaceous	Cu	Au	VMS	> 1 Mt – 2% Cu, 64 g/t Au
Rameshk	58.817	26.817	Gabbro, andesitic basalt and limestone	Upper Cretaceous-Lower Paleocene	Cu		VMS?	> 1 Mt
Anguran	47.406	36.628	Limestone, micaschist, and marble	Proterozoic	Pb, Zn	Ag	Carbonate-hosted	22 Mt – 24% Zn, 6% Pb
Alam kandi	47.283	36.717	Schist, marble, quartzite, and tuff	Proterozoic	Pb, Zn	Cu	Carbonate-hosted	~ 1 Mt – 7% Zn, 3% Pb
Ahangaran	48.991	34.186	Sandy dolomite, quartzite and shale	Lower Cretaceous	Pb, Zn	Fe, Ba, Cd, Ag	MVT	2Mt – 3% Pb, 1% Zn, 200 g/t Ag
Emarat	49.603	33.856	Limestone and dolomite	Cretaceous	Pb, Zn	Cu, Ag, Cd	MVT	10 Mt – 2% Pb, 3% Zn
Dona	51.450	36.165	Limestone and dolomite	Permian	Pb, Zn	Ba, Ag	Carbonate-hosted	6.5 Mt – 5% Pb, 1% Zn, 150 g/t Ag
Darreh noqreh	50.217	33.525	Limestone, pyroclastic and volcanic rocks	Cretaceous	Pb, Zn	Cu, Ag	MVT	~ 1 Mt – 21% Pb, 2% Zn, 150 g/t Ag

Deposits	Long	Lat	Host/country rocks	Stratigraphic age	Major Commodity	Other accessory minerals	Genetic type	Tonnage and grade
Lakan	50.648	33.109	Silicified limestone and shale	Cretaceous	Pb, Zn	Cu, Ag, Ba	SEDEX	5 Mt – 3% Zn, 4.5% Pb
Hosein abad	50.983	32.958	Black shale and sandstone	Jurassic	Pb, Zn		SEDEX	2 Mt – 1% Zn, 4% Pb
Anjeereh tiran	51.125	32.745	Dolomite, limestone, and shale	Cretaceous	Pb, Zn	Cu, Ag, Cd, Sb	MVT	1.5 Mt – 4% Zn, 1% Pb
Irankuh	51.625	32.500	Dolomite, limestone, and shale	Cretaceous	Pb, Zn	Ag, Cd	MVT	17 Mt – 11% Zn, 2.5% Pb
Kuh-e-surmeh	52.517	28.500	Dolomite, limestone, and sandstone	Lower Paleozoic	Pb, Zn		MVT	~ 1 Mt – 17% Zn, 2%Pb
Nakhlak	53.839	33.564	Limestone, shale, sandstone, and marl	Middle Triassic-Upper Cretaceous	Pb, Zn	Ag	MVT	3 Mt – 5% Zn, 75 g/t Ag
Moujen	54.658	36.525	Limestone	Permo-Triassic	Pb, Zn	Fe	MVT	~ 1 Mt – 2% Pb, 4% Zn
Khan jar	54.558	35.367	Dolomite and limestone	Cretaceous	Pb, Zn	Ag	Carbonate-hosted	1 Mt – 20% Pb, 4% Zn, 300 g/t Ag
Chah sorb	56.617	34.050	Dolomite and limestone	Middle Triassic	Pb, Zn	Ag	Carbonate-hosted	~ 1 Mt – 5% Zn, 2.5%Pb
Ozbak kuh	57.117	34.667	Limestone, shale, and sandstone	Paleozoic	Pb, Zn		Carbonate-hosted	2 Mt – 10% Zn, 4%Pb
Mehdi abad	55.025	31.483	Limestone, dolomite, and schist	Cretaceous	Pb, Zn	Fe, Ba	MVT	218 Mt – 7% Zn, 2.3% Pb, 51 g/t Ag
Koushk	55.775	31.733	Black shale	Proterozoic	Pb, Zn	Ag	SEDEX	5 Mt – 15% Zn, 3%Pb
Chah mir	56.042	31.65	Black siltstone	Late Cambrian	Pb, Zn		SEDEX	~ 1 Mt – 6% Zn, 3.5%Pb
Aghdarreh	47.017	36.667	Silicified limestone	Lower Miocene	Au	Sb, As, Hg	Sediment hosted	> 5 Mt – 4.5 g/t Au
Zarshuran	47.133	36.725	Dolomitic limestone and black shale	Upper Proterozoic-Lower Cambrian	Au	As, Sb, Hg, Zn	Sediment hosted	12 Mt – 7.9 g/t Au
Touzlar	47.466	36.833	Volcanic rocks	Oligo-Miocene	Au		Low sulfidation epithermal	~ 1 Mt – 3.1 g/t Au

Deposits	Long	Lat	Host/country rocks	Stratigraphic age	Major Commodity	Other accessory minerals	Genetic type	Tonnage and grade
Kervian	46.100	36.133	Meta-volcanic and schist	Mesozoic	Au		Orogenic gold	~ 1 Mt – 3 g/t Au
Alut	45.597	36.147	Quartz schist	Mesozoic	Au		Orogenic gold	~ 1 Mt – 2.5 g/t Au
Sari gunay	48.092	35.183	Porphyritic micro-diorite and rhyolite	Tertiary	Au	Sb, Cu, As, Hg	High sulfidation epithermal	108 Mt – 2.3 g/t Au
Astaneh	49.325	33.867	Micro-granite	Triassic-Jurassic	Au	Cu, W	Intrusion-related gold	~ 1 g/t Au
Muteh	50.608	33.667	Schist and meta-rhyolite	Upper Proterozoic-Lower Cambrian	Au	Cu	Epithermal	8 Mt – 3.2 g/t Au
Zarrin	54.625	32.675	Alluvium	Quaternary	Au	W	Placer	1 Mt - < 1 g/t Au
Kuh-e-zar	54.650	35.467	Alluvium	Quaternary	Au		Placer	~ 1 Mt – .05 g/t Au
Gandi	54.633	35.317	Volcano-sedimentary rocks	Eocene	Au	Cu, Pb, Zn, Ag	Intermediate epithermal	~ 1 Mt – 5 g/t Au
Zar mehr	58.927	35.174	Andesite and granodiorite	Eocene	Au		IOGC	1.5 Mt – 4 g/t Au
Zartorosht	57.211	28.219	Greenschist	Paleozoic	Au		Orogenic gold type	> 1 Mt – 3 g/t Au
Shahrak	47.828	36.420	Limestone, rhyodacite, and andesite	Oligo-Miocene	Fe		Volcanogenic	100 Mt – 57% Fe
Shams abad	49.725	33.817	Sandy dolomite and shale	Cretaceous	Fe	Mn, Cu	Volcanogenic	30 Mt – 47% Fe, 4% Mn
Sangan	60.400	34.408	Granodiorite, limestone and schist	Proterozoic	Fe		Skarn	900 Mt – 47% Fe
Robat posht badam	55.567	32.958	Gneiss, amphibolite, and marble	Triassic	Fe		Magmatic	> 1 Mt
Chador Malu	55.500	32.300	Meta-syenite, schist, and rhyolite	Proterozoic	Fe		Magmatic	450 Mt – 56% Fe
Sechahoon	55.643	31.718	Metasomatic granite, andesite, and tuff	Proterozoic	Fe		Magmatic	132 Mt – 35% Fe
Choghart	55.467	31.700	Syenite, schist, and rhyolite	Proterozoic	Fe	Mn	Magmatic	350 Mt – 55% Fe
Gol Gohar	55.083	29.267	Schist, marble, and quartzite	Proterozoic	Fe		Skarn	1200 Mt – 55% Fe

Deposits	Long	Lat	Host/country rocks	Stratigraphic age	Major Commodity	Other accessory minerals	Genetic type	Tonnage and grade
Tang-E-Zagh	56.017	27.950	Limestone and marl	Proterozoic	Fe	Mn	Sedimentary	5 Mt – 42% Fe, 1% Mn

4. Training dataset

The construction of the training database is conducted through the following multi-stage workflow: **1)** Compilation of publicly available geological and geophysical datasets, which are collected from authoritative references (Table 2); **2)** Feature enhancement through the use of edge-detection and gradient-based filters, which provide additional training features. These features highlight geological contrast and structural delineation; **3)** Target definition is a parameter that represents a metallogenic proxy. Here, the training target was generated based on the spatial density of mineral occurrence. This parameter illustrates the intensity and distribution of metallogenic intensity (Fig. 2); **4)** The training dataset was formed by compiling all training input databases (Table 2), which were sampled ore deposit locations (collected data in step 1). The training dataset represents the relevance of the geological or geophysical features to the training target.

The original compiled training dataset consists of 2351 sample points. Before any process, a certain data quality checking and data cleaning are required for preparing raw data for model training. To have high-quality data to make reliable predictions, the following steps are needed. (i) identifying and handling missing data, (ii) removing duplicates, (iii) handling outliers with unrealistic values of training features. If for one of the data points, all feature training data sets does not exist, that data point is removed. After visually checking the raw dataset and removing the problematic data points, the cleaned training data set with 2037 observation points was used to train the model.

The suggested database workflow supports a geologically informed and data-consistent training framework, crucial for generating robust and interpretable mineral prospectivity models throughout the Iranian plateau. Implementing ML-based mineral prospectivity mapping needs sophisticated methods for extracting meaningful and geologically plausible patterns from training datasets. A crucial prerequisite for achieving accurate model performance is ensuring compatibility and consistency in the format of training and the target features. The training features comprise diverse geoscientific datasets, each providing complementary insights into mineral systems. The widely used training features are geological data (e.g., Carranza, 2009; Li et al., 2021), geophysical data (e.g., Chen et al., 2015; Anderson et al., 2017), geochemical data (e.g., Soloviev et al., 2019; Xiong and Zuo, 2020), and remote sensing data (Bruzzone et al., 2006; Beygi et al., 2021; Shirmard et al., 2022). In the current study, the training features are geophysical measurements (Fig. 4; Table 2), mapped geological units (Fig. 5; Table 2), and spatial variation of the major lithospheric structures (Fig. 6; Table 2). The selected training feature datasets (Table 2) are underpinned by well-established geological principles and empirical evidence from the Iranian plateau's mineral systems. Each variable serves as a proxy for ore-controlling geological processes. For instance, proximity to igneous rock units indicates potential for porphyry Cu–Mo–Au and skarn-type Fe mineralization, especially within the Urumieh-Dokhtar magmatic arc, where Tertiary intrusions have been genetically linked to major deposits such as Sarcheshmeh and Meiduk (Aghazadeh et al., 2015). Similarly, specific lithological units such as rhyolite and dacite are associated with high-sulfidation epithermal gold systems and VMS deposits due to their arc volcanic origins. Mafic-ultramafic rocks (e.g., basalt, gabbro) present in ophiolitic belts act as host rocks for Cyprus-type VMS Cu–Zn deposits, like those found in SE Iran (Hajsadeghi et al., 2018). Structural features such as faults and fault density layers are included due to their role as conduits for hydrothermal fluids and their spatial association with Au and Cu deposits, particularly in the Sanandaj–Sirjan Zone (Aliyari et al., 2012). Moreover, stratigraphic layers reflecting Paleozoic and Mesozoic age units capture the metallogenic potential of formations that host Sedex Pb–Zn and MVT deposits (e.g., Koushk, Chahmir). These variables collectively reflect the regional metallotectonic framework shaped by Neo-Tethyan subduction and subsequent orogenesis, offering a geologically sound basis for mineral potential modelling. The geophysical data, including aeromagnetic and gravity datasets, are generally provided as continuous raster grids. These raster grids are composed of equally spaced square grids (pixels) and require minimal pre-processing for format alignment. For this study, all geophysical features were harmonized to a raster grid with a 2 km cell size, representing the resolution of spatial analysis. It is expected that the gravity and magnetic field and their derivatives highlight the effects of crustal scale faults and lineaments on the spatial distribution of ore deposits.

The geological features are provided primarily in vector formats of point data (e.g., ore deposits), polylines (e.g., faults and tectonic boundaries), and polygons (e.g., lithological units). Converting these to raster format enhances the visualization of their spatial relationships. This raster grid allocates each node or pixel the minimum distance to the nearest geological unit, facilitating a uniform and spatially obvious analysis. The transformation was implemented by calculating the Euclidean distance from each raster cell to the closest geological feature. The Euclidean distance is a standard metric for distance estimation of features in the GIS platforms, especially for MPM approaches. Thereby, the value of each point in the transformed raster grids represents the spatial proximity as a continuous variable throughout the grid.

The distribution of known mineral deposits across the study area is spatially irregular and sparse, often with a lack of comprehensive negative (non-mineralized) training examples. This heterogeneity and discontinuous dataset pose challenges for supervised ML approaches. To address this issue, a spatial density grid estimation of mineral deposits was applied to transform the discrete mineral deposit occurrence data into a continuous surface representing metallogenic intensity. The resulting spatial density grid has a raster grid format with a 2 km cell size to align with the training target.

Table 2
List of the geological and geophysical training feature layers.

Vector data (MD* raster grids), (This study)	**Raster grids**
Igneous rock units (IG_RU)	**Magnetic anomaly & derivatives**:
Ophiolite	Total magnetic intensity (TMI; Teknik et al, 2017)
Fault	Variable reduced-to-pole (VRTP) TMI, (This study)
Rhyolite	1st Vertical gradient of TMI VRTP, (This study)
Gabbro	1st x_horizontal gradient of TMI VRTP, (This study)
Granite	1st y_horizontal gradient of TMI VRTP, (This study)
Diabase	Analytical signal of TMI VRTP, (This study)
Diorite	ACMS**
Basalt	**Gravity anomalies** (Pavlis et al., 2012):
Dacite	Free Air gravity anomaly (FAA)
Cretaceous	Analytical signal of FAA, (This study)
Devonian	Bouguer gravity anomaly (BG)
Early Cretaceous	Analytical signal of BG, (This study)
Early Jurassic	**Gravity gradients components** ***
Early-Middle Triassic	Gxx
Early Paleozoic	Gxy
Eocene	Gxz
Eocene-Oligocene	Gyy
Late Cretaceous	Gyz
Cretaceous-Early Paleocene	Gzz
Late Eocene-Oligocene	**Elevation model** (Amante and Eakins, 2009)
Late Jurassic	Digital elevation model (DEM)
Late Jurassic-Early Cretaceous	1st Vertical gradient of DEM, (This study)
Late Paleozoic	1st x_horizontal gradient of DEM, (This study)
Middle Jurassic	1st y_horizontal gradient of DEM, (This study)
Miocene	Analytical signal of DEM, (This study)
Miocene-Pliocene	**Lithospheric major structures** *(*Irandoust et al., 2022):
Oligocene	Average Vs**** of upper crust, (This study)
Oligocene-Miocene	Average Vs**** of lower crust, (This study)
Ordovician-Silurian	Average Vs**** of upper mantle, (This study)
Paleocene	Depth to Moho
Paleocene-Eocene	**Miscellaneous**:
Permian	Easting coordinate
Pliocene	Northing coordinate

Vector data (MD* raster grids), (This study)	Raster grids
Pliocene-Quaternary	Earthquakes spatial density*****, (This study)
Precambrian	Fault lines (Sahandi and Soheili 2014) density
Quaternary	Density of boundaries of geological units, (This study)

** Minimum distance (calculated in this study) to the lithological units/ages (Sahandi and Soheili, 2014).*

***Averaged crustal magnetic susceptibility (*Teknik et al., 2020).

**** The gravity gradients for the study area are at an elevation of 225 km above the Earth's surface. The X-axis points to the north, the Y-axis points west, and the Z-axis points up (*Bouman et al., 2016).

*****Vs indicate shear velocity (*Irandoust et al., 2022).

****** The location of seismic events (Mw ≥ 3; from 1940) (*http://www.isc.ac.uk/isc-ehb/search/catalogue*).*

5. Methods

In this study, ML-based methodologies were implemented on the diverse geospatial datasets for predicting metallogenic potential zones across the Iranian plateau. The workflow commenced with the compilation and harmonization of multi-source geospatial data, including lithological, structural, geophysical, and geochemical layers. These datasets were preprocessed to ensure spatial coordinate consistency. Then, each layer of the dataset is structured into a comprehensive geospatial database to be suitable for supervised learning. For the construction of a structured database, an initial feature selection process was conducted to identify the most relevant training features for metallogenic systems by employing the Minimum Redundancy and Maximum Relevance (MRMR) algorithm (Ding and Peng, 2005). This process utilized statistical analysis and regression-based filtering methods to reduce dimensionality and the effects of the noisy features, essential for improving the efficiency of subsequent modeling processes. A variety of machine learning algorithms were employed to determine the most effective method for predicting areas with high metallogenic potential. Hyperparameters have been optimized for each algorithm through grid-search methods and validation feedback to enhance predictive accuracy. Hyperparameters are typically configuration variables that should be regulated manually to manage machine learning model before training. The hyperparameters are coefficient or mathematical functions that manage the layer number and the size of a neural network, for instance. The hyperparameters of the algorithms (e.g., the learning rate and the batch size) optimize the model learning processes from the data. The trained model on the selected geospatial features, was subsequently applied across the study area, enabling the generation of comprehensive mineral prospectivity maps.

In this study, we used three distinct datasets including a training dataset, 5-fold cross-validation, and an independent test set (Table S3). The training dataset consisted of 2037 spatial samples each associated with 69 geospatial features derived from geological, geophysical, and lithospheric features as listed in Table 2 and described in Section 4. This dataset was used to fit the regression models. Model performance was validated by 5-fold cross-validation procedure on the training dataset. This technique involved partitioning the 2037 samples of the training dataset into five subsets. Four subsets were used iteratively for training and one was reserved for validation in each iteration, thereby ensuring robustness and reducing overfitting of the models. Model performance was averaged across all folds and evaluated using RMSE and R^2 metrics. Additionally, we have an independent test set of 70 well-documented major ore deposits (listed in Table 1), which was used to qualitatively assess the correctness of our models. The 70 major ore deposits were not involved in the training or validation processes and were only used to evaluate how well the final model predicted the location of known big metallic mineral. This separation helps us to check how well the model works both on the data it was trained with and on the coordinate of unseen data.

Additionally, correlation and misfit metrics between the predicted and true occurrence of metallogenic intensity were conducted to assess model reliability. For the models with suboptimal performance (e.g., high RMS or low R^2 values), additional tuning was undertaken. This included removing outliers, refining hyperparameters, modifying feature selection criteria, and adjusting the optimization strategy to improve prediction accuracy and reduce model bias (Fig. 6).

Seven distinct ML algorithms with their 24 subtypes (Table S1), available in the MATLAB regression learner toolbox, were selected to represent a diverse range of algorithm families including tree-based, kernel-based, probabilistic, and neural network methods. The aim is to select an algorithm with optimal performance, suitable for MPM in the Iranian plateau. These major algorithms include: (i)

Linear Regression, (ii) Decision Tree, (iii) Vector Machine (SVM), (iv) Ensemble, (v) Gaussian Process Regression, (vi) Neural Network, and (vii) Kernel. Among these, Ensemble-based learning Methods, particularly those employing bagging (bootstrap aggregation), exhibited the most consistent and robust performance.

Ensemble learning methods integrate predictions from multiple base models to improve the overall prediction of the model by enhancing model accuracy and reducing variance. In this study, the Bagging ensemble method uses several base models on bootstrapped subsets of the training data in parallel. The base models are primarily neural network models. The final output was derived by aggregating the most frequent or average individual predictions of the base models (Fig. 6). The design and execution of this methodology were successfully used in the recent prospecting and exploration studies (e.g., Yin and Li, 2022; Chen and Chen, 2023; He et al., 2024). The application of the Bagging Ensemble method in this study not only enhanced predictive stability but also showcased its effectiveness in integrating geospatial and geophysical data for mineral prospectivity mapping (MPM).

Once the optimum model by tuning the hyperparameters is achieved, the trained model used to make predictions over regular grid nodes with a spatial resolution of 2 km × 2 km across the Iranian plateau. The cell size is selected based on the average resolution of the geophysical and geological raster grids. The gridded dataset has the same coverage as the aeromagnetic grid of Iran, which covers most of the plateau except for some gaps in the Zagros and Kopeh-Dagh regions (Teknik and Ghods, 2017; Teknik et al., 2020). We cast all datasets into a grid and name those as gridded datasets. It is important to note that this gridded dataset differs from the training feature dataset, which only includes sampling points located at known mineral occurrences. The training dataset consists of 2037 sampling points, while the gridded dataset consists of 377200 sampling points or grid nodes as summarized in Table S3. All the raster grids and rasterized grid layers were then resampled and aligned to the grid coordinate system, ensuring spatial and projection consistency with the training features and target variable, used for the final model prediction.

6. Results

An ML-based approach was developed to predict the spatial variation of metallogenic intensity. To achieve this, we integrated the spatial information of Fe, Cu, Pb, Zn, Au, Ag, and Mg into the metallogenic intensity dataset serving as a training target (Fig. 2b). This approach incorporated a comprehensive set of geophysical measurements and geological features (Table 2) as training datasets. The training datasets comprised 2,037 observation samples. Model performance was assessed through 5-fold cross-validation. Furthermore the validation is qualitatively assessed by using an independent observation point consisting of approximately 70 known metallic deposit locations. Model training was executed on MATLAB's machine learning toolbox using a system equipped with a 7-core Intel i7 GPU @ 2.8 GHz with 64 GB RAM. The training time is not equal for all models. The training models like Ensemble Bagged Trees and Neural Networks require more training time compared to simpler models like Linear Regression. The training was performed by using the parallel computing toolbox of MATLAB R2023b. The cross-validation and hyperparameter tuning were parallelized within loops and model-level parallel execution, which significantly reduced training time in the order of 3–5 hours, depending on hyperparameters variations.

An analysis of the training features' importance was conducted to evaluate the contribution of each training feature. Features with high importance alongside qualitative geological studies can enhance the accuracy of the prospective mapping. Moreover, it provides insights for the development of targeted exploration plans in the future as well as deepens our understanding of regional-scale ore formation processes. The Minimum Redundancy and Maximum Relevance (MRMR) algorithm (Ding and Peng, 2005) was used for feature importance analysis. The MRMR algorithm assesses the importance of each training feature on the stable prediction of the model, which is spatial mineralization density in this study. It works by reducing the redundancy among the training features while ensuring their high relevance to the prediction parameter. To achieve this, the mutual information is used to evaluate the features interaction with each other and their relevance to the prediction parameter of the model. Through the importance evaluation process, it removes each training feature from the training process and then estimates the accuracy parameters (e.g., R^2 and RMS) of the trained model. Reduction of the prediction accuracy of the trained model indicates the high importance of the removed training feature. The distribution of importance of the training features shown in Fig. 7 indicates that geological (e.g., density of fault lines) and some geophysical (e.g., magnetic and its derivatives) features exhibit high importance. The lithospheric features (e.g., Moho and seismic velocity variations) together with gravity anomalies have lower importance, likely due to their low spatial resolution.

Among the seven distinct ML algorithms with their 24 subtypes (Table S1), the Ensemble Bagged Trees algorithm demonstrated superior predictive accuracy, achieved by the highest coefficient of determination (R^2) of approximately 0.98 and the lowest root mean square error (RMSE) of about 0.03 (Table 3). The estimated mineral prospectivity map (Fig. 8) illustrates the spatial density of the mineral occurrence across the Iranian plateau, achieved by Ensemble Bagged Trees algorithm. The high correlation between predicted and the observed values ($R^2 \approx 0.98$) underscores the robust performance of the supervised Ensemble Bagged Trees algorithm (Fig. 9). The Bagged Trees algorithm is very similar to the Random Forest algorithms. Random Forest algorithms are successfully used for MPM (Carranza and Laborte, 2015; Parsa and Maghsoudi, 2021; Rodriguez-Galiano, et al. 2015; Yang, et al 2022). Therefore, it is not a surprise that we got the highest performance using Bagged Trees methods (Table S1 in the supplementary).

This regional-scale prospectivity map (Fig. 8) effectively identifies zones with known ore occurrences and predicts underexplored metallogenic zones that are primarily located in northwest, west, and Central Iran (Fig. 8). These prospective zones are predominantly associated with large-scale faults or major tectonic boundaries as well as magmatic complexes. Notably, the results indicate a southward extension of the high metallogenic potential of KaraDagh copper zone, in the northwest of the Iranian plateau. The southward extension is bounded by the NW-SE trending North Tabriz fault. Despite the limited number of training points, the model predicts spatial extension of the Malayer-Isfahan lead-zinc mineral zone toward the west, while a lower spatial density is anticipated eastward along the Kashan-Natanz metallogenic zone (Fig. 8). Additionally, areas nearby the central part of the Zagros suture zone located between Kermanshah and Neyriz ophiolites have been identified as potential targets for further exploration.

To highlight the underexplored metallogenic zones, a residual density map (Fig. 10) was calculated by subtracting the observed spatial mineralization density (Fig. 2b) from the predicted density of mineralization density (Fig. 8). This approach facilitates the identification of areas with high metallogenic potential that have not yet been thoroughly investigated. Interestingly, this residual prediction identifies three significant potential metallogenic zones, indicating new prospective areas in the northwest, western, and northern parts of the Iranian plateau.

Table S1

The results are achieved for ML methods. RMSE is the root mean squared error on the validation set. The metrics of R-squared (R2) indicates how well the predicted results explain the target of training. MAE is the Mean absolute error. The MAE is always positive and similar to the RMSE, but less sensitive to outliers. MSE represents mean squared error. The list is sorted in ascending order of RMSE and descending order of R-squared values.

Methods Type	Subtype	RMSE (Validation)	MSE (Validation)	RSquared (Validation)	MAE (Validation)
Ensemble	Bagged Trees	0.03125	0.00100	0.97620	0.01809
Gaussian Process Regression	Matem 5/2 GPR	0.03272	0.00107	0.97245	0.01818
Gaussian Process Regression	Rational Quadratic GPR	0.03286	0.00108	0.97221	0.01821
Gaussian Process Regression	Squared Exponential	0.03337	0.00111	0.97133	0.01850
Neural Network	Bi-layered NN	0.03637	0.00132	0.96595	0.02410
Neural Network	Tri-layered NN	0.03979	0.00158	0.95924	0.02600
Gaussian Process Regression	Exponential	0.04054	0.00164	0.95770	0.02379
Neural Network	Medium NN	0.04410	0.00194	0.94995	0.02773
SVM	Cubic	0.04447	0.00198	0.94909	0.02742
Kernel	SVM	0.04651	0.00216	0.94432	0.02977
Neural Network	Wide NN	0.04832	0.00234	0.93989	0.02886
SVM	Quadratic	0.04948	0.00245	0.93699	0.03293
Neural Network	Narrow	0.05437	0.00296	0.92391	0.03477
SVM	Medium Gaussian	0.05508	0.00303	0.92190	0.03575
Tree	Fine Tree	0.05723	0.00328	0.91569	0.03054
Kernel	Least Squares Regression kernel	0.05964	0.00356	0.90843	0.04204
Tree	Medium	0.06426	0.00413	0.89369	0.03781
Ensemble	Boosted Trees	0.06535	0.00427	0.89008	0.05057
Tree	Coarse Tree	0.08223	0.00676	0.82594	0.05707
SVM	Fine Gaussian	0.09723	0.00945	0.75665	0.05928
Linear Regression	Linear	0.11999	0.01440	0.62938	0.09175
SVM	Linear	0.15443	0.02385	0.38612	0.09373
SVM	Coarse	0.17181	0.02952	0.24011	0.10043
Linear Regression	Robust	0.17434	0.03039	0.21760	0.09108
.					

Table S2
Summary of ML Model Hyperparameters and Tuning Ranges

Model Type	Subtype	Key Hyperparameters	Tuning Ranges / Notes
Ensemble (Bagged Trees)	Bagged Trees	NumLearningCycles, MinLeafSize	NumLearningCycles: 30; MinLeafSize: 8
Gaussian Process	Matern 5/2 Kernel	KernelScale, Sigma, BaiscFunction,	KernelScale: auto (fitrgp default), Sigma: auto, BasicFunction: constant
Neural Network	Tri-layered Feedforward	NumHiddenLayers, NeuronsPerLayer, LearningRate	Layers: 3 (fixed); Neurons: 10–100 per layer; LearningRate: 0.001–0.05
SVM	Cubic	BoxConstraint, KernelScale	BoxConstraint: 0.1–100; KernelScale: 0.01–10
Kernel Regression	SVM Kernel	KernelFunction, Regularization, andIterationLimit	KernelFunction: 'gaussian'; Regularization: 0.001–1; IterationLimit: 1000
Decision Tree	Fine Tree	Surrogate decision splits, MinLeafSize	Surrogate decision splits: off; MinLeafSize : 1–5 (optimized at 4)
Linear Regression	Linear	None (least-squares solution)	Robust option: on
Note: All the models were trained using MATLAB R2023b functions with custom tuning via grid search. The final parameters were selected using 5-fold cross-validation for minimizing RMSE.			

Table 3
The higher metrics results are achieved for the selected seven different ML methods. The metrics of root mean squared error (RMSE) and R-squared (R2) indicate how well the predicted results explain the target of training. The list is sorted in ascending order of RMSE and, simultaneously, in descending order of R-squared values. The training point number of observations is 2037 with 69 training features or predictors. Validation of the training results is tested with the 5-fold cross-validation. The optimum result is achieved with the Ensemble Bagged Trees method. For details of the training metrics results see Table S1. The best predicted spatial density of the ore occurrences across the model achieved by the Ensemble Bagged Trees method is shown in Fig. 8. The predictive model for the six other models is presented in Figures S1 to S6 in the supplementary.

Num.	Method	Sub Type	RMSE (Validation)	R_Squared (Validation)
1	**Ensemble**	**Bagged Trees**	0.031	0.98
2	Gaussian Process Regression	Matem 5/2	0.033	0.97
3	Neural Network	Trilayered	0.040	0.96
4	SVM	Cubic	0.044	0.95
5	kernel	SVM	0.046	0.94
6	Tree	Fine	0.057	0.91
7	Linear Regression	Linear	0.119	0.62

Table S3
Summary of Data Flow

Dataset	Size	Purpose	Used For
Training Dataset	2037	Model learning	Regression modeling
Validation (Cross validation folding)	5 subsets of training data	Hyperparameter tuning & model selection	RMSE/R^2 evaluation
Independent Test Set	70	External model validation	Final qualitatively asses of the trained model
Gridded dataset	377200	Apply the trained model on the nodes of the grid	Prediction map across the study area with a 2 km × 2 km.

7. Discussion

7.1. The mineral prospectivity mapping algorithmic perspective

The data-driven approach of mineral prospectivity mapping (MPM) introduces regional-scale exploration solutions by integrating multidimensional geospatial dataset. This geospatial dataset typically consists of various geological features (e.g., rock units and fault lines), lithospheric parameters (e.g., Moho depth and seismic velocity heterogeneity of different layers of the lithosphere), and geophysical measurements (e.g., gravity, magnetic, and their respective derivatives). All of those heterogenous features merged into a unified training dataset. A set of supervised regression-based algorithms are used to derive a predictive model for delineating high-potential metallogenic zones across the Iranian plateau. Using seven major ML algorithms with their 24 subtypes of MATLAB regression learner toolbox, the Ensemble Bagged Trees algorithm performed more accurate and stable predictions for mineral prospectivity across the Iranian plateau, as evidenced with the lowest validation RMSE (~ 0.03), highest R^2 (~ 0.98) on other metrics (See details at Table S1 in the supplementary). The algorithm inherently has abilities of variance reduction, robustness to overfitting, and handling high-dimensional non-linear geospatial data (e.g., Yin and Li, 2022; Chen and Chen, 2023; He et al., 2024).

Bagging or bootstrap aggregation lunches multiple decision trees using random subsets of the training data set and then aggregates their outputs to one solution. This approach reduces the potential high variance in the prediction of decision trees by averaging the predictions of all trees. Therefore, using this technique leads to a robust prediction model that is less sensitive to outlier prediction. In our study, the 69 training features represents complex and diverse geological, geophysical, and lithospheric ore-forming controlling parameters. This kind of multidimensional and often spatially noisy data can lead to overfitting in the individual learners. The Bagged Trees method enhances model stability by capturing the dominant prediction without being highly influenced by localized anomalies. The model's ability to derive the non-linear relationships between the training target of ore deposits spatial density and training features is essential for accurate prediction. The strong performance was observed in the cross-validation results. Moreover, the high spatial correlation of the independent 70 major deposit with areas of high values of the predicted density of mineralization, qualitatively provided extra assessment of the performance of the employed model.

The Ensemble Bagged Trees algorithm shows the relatively accurate prediction of mineralization density, which is important for real-world mineral prospecting mapping. Importantly, this method aligned well with the goals of our study to detect underexplored metallogenic zones. The algorithm's predictive strengths helped us to delineate new potential zones across a geologically complex and tectonically active region of Iranian plateau with diverse types of metallogenic zones, which made the prediction geologically interpretable and highly suitable for regional-scale mineral prospectivity mapping.

7.2. Limitations and challenges of ML-driven mineral prospective mapping

Although the employed ML-driven prospective mapping enhances exploration efficiency in detecting high-potential metallogenic zones, it is essential to recognize its limitations to ensure accurate interpretation. The predictive accuracy of these models is fundamentally dependent on the quality, resolution, and temporal relevance of both training and target datasets (Farahnakian et al., 2024). For instance, the dataset of ore deposits used in this study is limited to the most recent (2017 and later) discovered ore deposits. Consequently, the results should be interpreted cautiously, with an awareness of potential gaps or outdated information that may affect the accuracy and comprehensiveness of the analysis (Singer, 2007; Mateus and Martins, 2019).

It is crucial to integrate all deposit types as a unique training target data set; otherwise, prediction by individual AI predictive models would be impossible. By considering metallogenic intensity (spatial density of the ore deposits) parameter, we made a unified model of the diverse types of the seven selected ore deposits. Our approach treats the spatial density of all types of ore deposits as a proxy for metallogenic intensity parameter. This means that metallogenic intensity or spatial density of metallogeny across the plateau, structurally and lithologically associated with the same crustal-scale processes (e.g., Sun et al., 2020).

While different ore deposit types (e.g., porphyry, skarn, vein, SEDEX, MVT) are genetically distinct, but they may still occur within shared mineralisation systems that are governed by common lithospheric-scale processes, including magmatism-related sources, faulting, fluid flow pathways, and depositional environments (McCuaig and Hronsky, 2017). Following the mineral systems approach (e.g., Hronsky and Groves, 2008; McCuaig et al., 2010), we argue that these different ore deposits can be regionally associated as an unique parameter, due to their formation within large-scale crustal architectures that condition the source, transport, and focusing of mineralizing fluids. By considering this argument, the similar evidences of different types of ore deposits can be tracked in the geological, geophysical and geochemical observations (Rodriguez-Galiano et al., 2015).

Recent mineral system analysis is gradually accepting this approach in ore genesis studies. However, the conceptual framework of linking the mineral system to available data sets is still under development (McCuaig et al., 2010; Tagwai et al., 2024). While the mineral exploration studies have recognised the approach of this study as useful for the for prospecting metallogenic zones by investigation of ore formation processes (Knox-Robinson and Wyborn, 1997; Groves et al., 2022; Tagwai et al., 2024), using the spatial density as a proxy for mineralization intensity is not intended to imply genetic uniformity, but rather to model the cumulative metallogenic potential imparted by tectonomagmatic controls. This strategy enables us to capture regional mineralization patterns without violating the theoretical distinctions between deposit types. Our results support this view, as spatially clustered mineralization zones align with known trans-lithospheric faults, magmatic arcs, and high-relief tectonic boundaries—structural features widely recognized as metallogenic drivers.

Despite these limitations, the MPM approach offers an organized approach that prioritizes data-driven targets, minimizes expenses, and enhances discovery rates. To prevent over-interpretation, it is essential to acknowledge the limitations of the input datasets. Integrating advanced ML techniques with high-quality updated geospatial data enables MPM to optimize exploration strategies and enhance the likelihood of successful ore deposit explorations (Zhang et al., 2024).

A central challenge in this study arises from the irregular distribution of the discovered ore deposits (Fig. 2), which underscores both the geological complexity of the Iranian plateau and the influence of historically biased exploration efforts (Lou and Liu, 2023). The observed spatial pattern, marked by clustering and sparsity, highlights the challenges of directly attributing raster grid training features to discrete deposit locations due to the variable intensity of the mineralization. The irregular spatial distribution of the ore deposits can cause less uncertain prediction, especially where the distribution is sparse or different ore deposits are highly clustered. To overcome these limitations and align with advancements in handling imbalanced geospatial data, the spatial density of the mineral deposits is selected as the target variable for ML model, instead of depending on specific mineral deposit coordinates (Farahnakian et al., 2024). To evaluate the spatial uncertainty of the predictions, a residual map (Figure S7) was generated, showing the difference between true and predicted spatial densities of ore deposits at known locations. Residuals mostly fall within ± 0.1, suggesting good model performance overall. However, larger residuals (>|±0.1|) are observed in under-sampled areas, indicating greater model uncertainty. These residuals are particularly notable for isolated deposits distant from major metallogenic clusters. Interestingly, even in some highly sampled regions, such as the KaraDagh metallogenic zone in the northwest of the Iranian plateau, a localized cluster of elevated residuals is detected, possibly due to local geological complexity.

Relatively low feature importance scores of lithospheric and gravity features (e.g., Moho, crustal seismic velocity, and Bouguer gravity anomalies) are in contrast with the generally accepted importance of lithospheric structures in controlling metallogenic zones. The Moho depth and Bouguer anomalies have spatially low resolution (~ > 0.5°). These low-resolution lithospheric features contribute less to localized variance of the metallogenic spatial density (Fig. 7). However, in this study qualitatively and less quantitatively, they still provide important geological context by delineating major crustal domains, tectonic boundaries, and zones of magmatic activities, all of which influence ore-forming processes.

It is worth noting that the ore deposits dataset used here was last updated in 2017. Therefore, any exploration conducted since then could be vital in independently validating or refining our predictions. Therefore, newly identified ore occurrences would provide valuable ground-truth evidence for the model's reliability and help fine-tune prospectivity interpretations.

7.3. Geological implications of the results

The suitable condition for the formation of metallic ore deposits is inherently associated with a specific physicochemical condition, geodynamic processes, and tectonic evolution. Therefore, the spatial mineral occurrences are typically attributed to the geological features (e.g., lithological units, fault systems, magmatic intrusions, and hydrothermal fluids). The geophysical anomalies (e.g., gravity and magnetic) reflect those geological structures, depending their sensitivity. These complex ore deposit formation mechanisms within various types of geological structures and their complicated geophysical signatures pose significant challenges to regional metallogenic zone mapping (Chernicoff et al., 2002; Bierlein et al., 2006; Leclerc et al., 2012; Dufréchou et al., 2015; Jamali and Mehrabi, 2015; Bauer et al., 2022).

The residual spatial density of the mineral deposits (Fig. 10) was derived by subtracting the calculated spatial density of the ore deposits (Fig. 2a) from the model's prediction (Fig. 8). The residual density map provides insights to pinpoint areas across the Iranian plateau with high metallogenic potential, which have remained underexplored. The results indicate that the promising areas are closely associated with the known major metallogenic zones (Fig. 10). The residual anomalies are spatially aligned with established metallogenic provinces, such as the KaraDagh, Malayer-Isfahan, and Toroud zones (see Figs. 2d and 10). This pattern indicates that the model accurately represents the main litho-structural and magmatic-tectonic controls on ore formation in the region. The zones lie within geodynamically active regions shaped by the convergence of the Arabian and Eurasian plates, where processes such as crustal shortening, strike-slip faulting, and arc magmatism have historically facilitated the formation of systems including porphyry Cu-Au-Mo ore deposits. The Central Iran block (e.g., Yazd, Tabas, and Lut blocks) exhibits comparatively weak residual signals, which presumably indicates that significant mineralized belts in this region have been well-mapped by previous explorations. However, some limited, structurally aligned anomalies trace the terrane boundaries and mapped faults. This observation highlights the significance of deep crustal fractures in directing hydrothermal fluids in central Iran. We argue that the distribution of ore deposits is not controlled only by active faults but controlled by all crustal scale fractures, old faults, and inactive lineaments. A better fault and lineament map will affect our results to be more precise but because of using a coarse fault map, the effect of all crustal-scale faults and fractures is missing in our results. However, the topography and magnetic field with their derivatives may provide the expected effect of those crustal-scale cracks, old faults, and inactive lineaments, which are not presented in the fault map of Iran.

Especially, the high feature importance of the DEM (Digital Elevation Model) layer (Fig. 7) and its derivatives indicate its typical correspondence to the tectonically active regions such as fault zones, terrane boundaries, suture zones and magmatic intrusions, which are spatially associated with ore deposit (e.g., porphyry Cu, skarn, epithermal Au) (e.g., Yang et al., 2022; Zuo and Xu, 2023). Therefore, the high feature importance of topography does not imply that elevation causes mineralization, but instead the DEM acts as a proxy variable that captures the spatial pattern of geological processes, which are conducive to ore deposit formation. For instance, in the Iranian plateau, the Urumieh-Dokhtar magmatic arc, important for hosting porphyry and skarn deposits, is marked with high relief originating from intense subduction-related magmatism. The prospectivity maps also hold relevance for critical minerals of rare earth elements, which are often genetically related to metallic ore-forming systems (e.g., Petrella et al., 2014; Zarasvandi et al., 2015; Abedini et al., 2023).

7.4. AI-methods potentials for MPM and suggestions for future studies

This study indicates the efficiency of applying modern ML algorithms on the various geospatial data for prospecting metallogenic zones on a regional scale, especially in areas with diverse tectonics, such as Iranian plateau. Employing this approach provided valuable regional insights into potential metallogenic zones by including only positive training dataset. Positive training data points indicate observation points with confirmed mineralization, while negative data points represent locations where ore deposit formation is unlikely. The applicability of the AI-driven approaches can be broadened through the integration of advanced deep learning methods by including both positive and negative training datasets. The aim is to provide interpretable AI-aided algorithms in mineral exploration with a promising trajectory in MPM. Enhancing the workflow by using new ML methods alongside advanced hyperparameter optimization would help mitigate overfitting and more effectively manage non-linearity problems between training dataset and the target of the method (Chen and Wu, 2017; Li et al., 2021, 2024; Maepa et al., 2021; Parsa and Carranza, 2021; Parsa and Maghsoudi, 2021; N. Yang et al., 2022; Yin et al., 2023; Zuo and Xu, 2023; Wake et al., 2024).

To achieve a trained model with higher prediction accuracy, it is essential to incorporate diverse geospatial datasets with higher resolution. For instance, integration of radiometric and geochemical sampling together with satellite-driven multispectral or hyperspectral imagery can significantly improve the prediction accuracy of the trained model. These additional datasets, especially hyperspectral images, identify hydrothermal alteration indicators, geochemical anomalies, and structurally controlled mineralizing systems. Applying this approach will enhance the model sensitivity to characteristics such as iron zones, clay alteration, or silicification, which typically indicative of deposit types like porphyries, epithermal systems, or skarns.

While this study focused on identifying prospective metallogenic zones, regardless of mineralization type, the workflow could be adapted to distinguish deposit types by classification learning algorithms using spectral, geophysical, or geochemical training dataset (Abedi et al., 2012; Shirmard et al., 2022; Chen and Chen, 2023; Farahnakian et al., 2024; Mahboob et al., 2024). For example, segmentation algorithms could relatively differentiate porphyry copper systems, characterized by halos and disseminated sulfides alteration, from epithermal gold-silver deposits, which are marked by alteration zones of vein-hosted metallogenic and intense silicification (Shayeganpour and Tangestani, 2022; Amraoui et al., 2025; Farahbakhsh et al., 2025). Employing such approaches would facilitate more precise targeting of specific deposit types. These approaches, when properly implemented, would yield significant insights into spatial patterns of the ore deposits, thereby enhancing mineral exploration strategies and decision-making processes.

8. Conclusions

The AI-aided mineral prospectivity mapping (MPM) approach is used to identify new metallogenic zones in the Iranian plateau. Analyzing regional-scale geological and geophysical data is typically associated with challenges when using traditional methods. AI algorithms facilitate resolving the nonlinear and complex patterns among irregularly distributed mineral deposits using multimodal geological and geophysical big data. Regression learning methods are used to identify the intrinsic relationship between various geological and geophysical training features and the locations of the metallic ore deposits as training targets.

The training target dataset is formed by integrating the location of seven metallic ore deposits including Fe, Cu, Pb, Zn, Au, Ag, and Mg. Then the spatial density of ore deposits is computed using the integrated dataset. The information regarding the grade and tonnage of various ore deposits in our dataset is limited, thus identical importance weights are assigned to each ore deposit. To form training feature dataset, the vector-based features (e.g., lithological units and fault lines) were transformed into a set of raster grids to ensure their data format consistency with geophysical and lithospheric raster grids. The raster grids and vector-based features are created by calculating the minimum distance to geological units and lithospheric structural boundaries. These created raster grids together with raster grids of geophysical measurements and mid-lithospheric interfaces (e.g., average crustal shear waves and Moho depth), formed the training dataset comprising 69 features. Feature importance analysis is conducted to identify the most relevant features for ore formation.

The learning performance is evaluated for seven major regressions-based algorithms with their subtypes reaching 24 methods. The Ensemble Bagged Trees method displayed the best performance. The selection criteria were the minimum RMSE (~ 0.03) and maximum R-Squared ($R^2 \approx 0.98$) value from the regression analysis of prediction versus observation of validation data. Once the model is trained and its accuracy adheres to the acceptable critical, it is employed to estimate the spatial density of the ore occurrences at grid nodes with a cell spacing of 2 km across the Iranian plateau. The predicted spatial density of the ore deposits is compared with locations of comprehensive data on world-class ore deposits. To highlight underexplored areas, residual spatial density anomalies were calculated by subtracting the observed from the predicted spatial density. The results indicate the prediction is optimally aligned with the spatial association of major ore deposits. The trends of predicted spatial density indicates a new zone of metallogenic activity close to the existing metallogenic zones. This study suggests that the structural boundaries and magmatic complexes along with geophysical observations, are significant indicators of metallic ore deposits and should be prioritized in future mineral exploration plans.

The results indicate that the high-potential metallogenic zones are primarily located in the northwest of the study area, aligning closely with the known distribution of the Copper metallogenic zone of the KaraDagh. The southern boundary of this zone is primarily outlined by the major North Tabriz fault. The predicted area on the western side of the Zagros suture aligns closely with the known Malayer-Isfahan Pb-Zn metallogenic zone. The residual spatial density of the ore deposits suggests that Central Iran has already been almost fully explored, revealing fewer unexplored metallogenic zones. Nonetheless, a locally less explored metallogenic zone has been identified near the Bafgh, Nehbandan-Ferdous, and Jiroft-Shaherbabak metallogenic zones.

The results of this study are useful for enhancing local-scale exploration success by employing a practical and multidisciplinary workflow of reginal-scale mineral prospective mapping (MPM). This approach addresses the rising demands for ore minerals, considering sustainable development and the economic limitations of mineral exploration. Leveraging the recent advancements in the big data analysis and artificial intelligence algorithms aid environmentally sustainable mineral exploration.

Declarations

Data/Software availability statement

The National Centers for Environmental Information (https://www.ncei.noaa.gov/products/etopo-global-relief-model) was used to access the ETOPO1 global elevation model (Amante and Eakins, 2009) from the ETOPO Global Relief Model grid. The Cenozoic volcano's locations are downloaded from the Smithsonian Institution's Global Volcanism Program (GVP) website (https://volcano.si.edu/). The gravity gradient grids at 225 km and 255 km height are available from the website of the European Space Agency (ESA) (https://earth.esa.int/eogateway/catalog/goce-global-gravity-field-models-and-grids) (Bouman et al., 2016). The EGM2008 global Bouguer anomaly model (Pavlis et al., 2012) has been accessed by the National Geospatial-Intelligence Agency from the website (https://bgi.obs-mip.fr/grids-and-models-2/grids-and-models-2-2/#toc7). The MATLAB codes are used to prepare data and compute the models that can be provided by the author. The lithological units/ages (Sahandi and Soheili 2014). Averaged crustal magnetic susceptibility (Teknik et al. 2020). Vs indicate shear velocity (Irandoust et al., 2022). The location of seismic events (Mw ≥ 3; from 1940) (http://www.isc.ac.uk/isc-ehb/search/catalogue).

Conflict of Interest

The authors have no conflicts of interest to declare that are relevant to the content of this article

Acknowledgments

This research received no specific grant from any funding agency in the public, commercial, or not-for-profit sectors. Vahid Teknik (VT) extends his special appreciation to Ebrahim Gholamzadeh, whose support made this research possible. VT thanks Irina Artemieva and Hans Thybo for helpful scientific support. Amr Abdelnasser extends his appreciation to the Scientific Research Project (BAP Project ID: 46804) at Istanbul Technical University (ITU, Turkey).

References

1. Abedi M, Norouzi GH, Bahroudi A (2012) Support vector machine for multi-classification of mineral prospectivity areas. Comput Geosci 46:272–283. https://doi.org/10.1016/j.cageo.2011.12.014
2. Abedini M, Ziaii M, Timkin T, Pour AB (2023) Machine Learning (ML)-Based Copper Mineralization Prospectivity Mapping (MPM) Using Mining Geochemistry Method and Remote Sensing Satellite Data. Remote Sens 2023 15(15):3708. https://doi.org/10.3390/RS15153708
3. Adiri Z, Lhissou R, El Harti A, Jellouli A, Chakouri M (2020) Recent advances in the use of public domain satellite imagery for mineral exploration: A review of Landsat-8 and Sentinel-2 applications. Ore Geol Rev 117. https://doi.org/10.1016/j.oregeorev.2020.103332
4. Aghazadeh M, Hou Z, Badrzadeh Z, Zhou L (2015) Temporal-spatial distribution and tectonic setting of porphyry copper deposits in Iran: Constraints from zircon U-Pb and molybdenite Re-Os geochronology. Ore Geol Rev 70:385–406. https://doi.org/10.1016/J.OREGEOREV.2015.03.003
5. Alaminia Z, Karimpour MH, Homam SM, Finger F (2013) The magmatic record in the Arghash region (northeast Iran) and tectonic implications. Int J Earth Sci 102:1603–1625. https://doi.org/10.1007/s00531-013-0897-1
6. Alavi M (1996) Tectonostratigraphic synthesis and structural style of the Alborz Mountain System in Iran. J Geodyn 21:1–33
7. Aliyari F, Rastad E, Mohajjel M (2012) Gold Deposits in the Sanandaj-Sirjan Zone: Orogenic Gold Deposits or Intrusion-Related. Gold Systems? Resource Geol 62:296–315. https://doi.org/10.1111/J.1751-3928.2012.00196.X;PAGEGROUP:STRING:PUBLICATION
8. Allen MB, Kheirkhah M, Neill I, Emami MH, Mcleod CL (2013) Generation of Arc and Within-plate Chemical Signatures in Collision Zone Magmatism: Quaternary Lavas from Kurdistan Province, Iran. J Petrol 54:887–911. https://doi.org/10.1093/petrology/egs090
9. Amante C, Eakins BW (2009) ETOPO1 1 Arc-Minute Global Relief Model: Procedures, Data Sources and Analysis, NOAA Technical Memorandum NESDIS NGDC-24. https://doi.org/10.1594/PANGAEA.769615
10. Amraoui T, Ibouh H, Farah A, Bammou Y, Shebl A (2025) Remote sensing mapping of structural and hydrothermal alteration in the mougueur inlier, Eastern high atlas, Morocco. Sci Rep 15:1–18. https://doi.org/10.1038/S41598-025-99402-0;SUBJMETA=213,2151,330,431,704;KWRD=GEOLOGY,MINERALOGY,PETROLOGY

11. Anderson ED, Monecke T, Hitzman MW, Zhou W, Bedrosian PA (2017) Mineral Potential mapping in an accreted island-Arc setting using aeromagnetic data: An example from Southwest Alaska. Econ Geol 112:375–396. https://doi.org/10.2113/ECONGEO.112.2.375
12. Arjmandzadeh R, Karimpour MH, Mazaheri SA, Santos JF, Medina JM, Homam SM (2011) Sr-Nd isotope geochemistry and petrogenesis of the Chah-Shaljami granitoids (Lut Block, Eastern Iran). J Asian Earth Sci 41:283–296. https://doi.org/10.1016/J.JSEAES.2011.02.014
13. Asadi S, Moore F, Zarasvandi A (2014) Discriminating productive and barren porphyry copper deposits in the southeastern part of the central Iranian volcano-plutonic belt, Kerman region, Iran: A review. Earth Sci Rev 138:25–46. https://doi.org/10.1016/J.EARSCIREV.2014.08.001
14. Bagheri H (2015) Crustal lineament control on mineralization in the Anarak area of Central Iran. Ore Geol Rev 66:293–308. https://doi.org/10.1016/J.OREGEOREV.2014.10.028
15. Bauer TE, Lynch EP, Sarlus Z, Drejing-Carroll D, Martinsson O, Metzger N, Wanhainen C (2022) Structural Controls on Iron Oxide Copper-Gold Mineralization and Related Alteration in a Paleoproterozoic Supracrustal Belt: Insights from the Nautanen Deformation Zone and Surroundings, Northern Sweden. Econ Geol 117:327–359. https://doi.org/10.5382/ECONGEO.4862
16. Benaissi L, Tarek A, Tobi A, Ibouh H, Zaid K, Elamari K, Hibti M (2022) Geological mapping and mining prospecting in the Aouli inlier (Eastern Meseta, Morocco) based on remote sensing and geographic information systems (GIS). China Geol 5:614–625. https://doi.org/10.31035/cg2022035
17. Berberian M, King GCP (1981) Towards a paleogeography and tectonic evolution of Iran. Can J Earth Sci 18:210–265. https://doi.org/10.1139/e81-019
18. Bergen KJ, Johnson PA, de Hoop MV, Beroza GC (2019) Machine learning for data-driven discovery in solid Earth geoscience. Science (1979) 363. https://doi.org/10.1126/science.aau0323
19. Beygi S, Talovina IV, Tadayon M, Pour AB (2021) Alteration and structural features mapping in Kacho-Mesqal zone, Central Iran using ASTER remote sensing data for porphyry copper exploration. Int J Image Data Fusion 12:155–175. https://doi.org/10.1080/19479832.2020.1838628
20. Bierlein FP, Groves DI, Goldfarb RJ, Dubé B (2006) Lithospheric controls on the formation of provinces hosting giant orogenic gold deposits. Min Depos 40:874–886. https://doi.org/10.1007/S00126-005-0046-2
21. Boulin J (1991) Structures in Southwest Asia and evolution of the eastern Tethys. Tectonophysics 196:211–268. https://doi.org/10.1016/0040-1951(91)90325-M
22. Bouman J, Ebbing J, Fuchs M, Sebera J, Lieb V, Szwillus W, Haagmans R, Novak P (2016) Satellite gravity gradient grids for geophysics. Sci Rep 6:1–11. https://doi.org/10.1038/srep21050
23. Bruzzone L, Chi M, Marconcini M (2006) A novel transductive SVM for semisupervised classification of remote-sensing images. IEEE Trans Geosci Remote Sens 44:3363–3373. https://doi.org/10.1109/tgrs.2006.877950
24. Burg JP (2018) Geology of the onshore Makran accretionary wedge: Synthesis and tectonic interpretation. Earth Sci Rev 185:1210–1231. https://doi.org/10.1016/j.earscirev.2018.09.011
25. Carranza EJM (2009) Controls on mineral deposit occurrence inferred from analysis of their spatial pattern and spatial association with geological features. Ore Geol Rev 35:383–400. https://doi.org/10.1016/j.oregeorev.2009.01.001
26. Carranza EJM, Laborte AG (2015) Random forest predictive modeling of mineral prospectivity with small number of prospects and data with missing values in Abra (Philippines). Comput Geosci 74:60–70. https://doi.org/10.1016/j.cageo.2014.10.004
27. Chen G, Cheng Q, Zuo R, Liu T, Xi Y (2015) Identifying gravity anomalies caused by granitic intrusions in Nanling mineral district, China: a multifractal perspective. Geophys Prospect 63:256–270. https://doi.org/10.1111/1365-2478.12187
28. Chen J, Chen Y (2023) A high-performance voting-based ensemble model of graph convolutional extreme learning machines for identifying geochemical anomalies related to mineralization. Ore Geol Rev 162:1–14. https://doi.org/10.1016/j.oregeorev.2023.105706
29. Chen Y, Wu W (2017) Mapping mineral prospectivity using an extreme learning machine regression. Ore Geol Rev 80:200–213. https://doi.org/10.1016/j.oregeorev.2016.06.033
30. Chernicoff CJ, Richards JP, Zappettini EO (2002) Crustal lineament control on magmatism and mineralization in northwestern Argentina: Geological, geophysical, and remote sensing evidence. Ore Geol Rev 21:127–155. https://doi.org/10.1016/S0169-

1368(02)00087-2

31. Chiu HY, Chung SL, Zarrinkoub MH, Mohammadi SS, Khatib MM, Iizuka Y (2013) Zircon U-Pb age constraints from Iran on the magmatic evolution related to Neotethyan subduction and Zagros orogeny. Lithos 162–163:70–87. https://doi.org/10.1016/J.LITHOS.2013.01.006
32. Chukwu C, Betts P, Moore D, Munukutla R, Armit R, McLean M, Grose L (2024) Unsupervised machine learning and depth clusters of Euler deconvolution of magnetic data: a new approach to imaging geological structures. Explor Geophys 55:223–245. https://doi.org/10.1080/08123985.2023.2299475
33. Daliran F (2008) The carbonate rock-hosted epithermal gold deposit of Agdarreh, Takab geothermal field, NW Iran - Hydrothermal alteration and mineralisation. Min Depos 43:383–404. https://doi.org/10.1007/S00126-007-0167-X
34. Davies RS, Davies MJ, Groves D, Davids K, Brymer E, Trench A, Sykes JP, Dentith M (2021) Learning and Expertise in Mineral Exploration Decision-Making: An Ecological Dynamics Perspective. Int J Environ Res Public Health 18:9752. https://doi.org/10.3390/ijerph18189752
35. Dentith M, Enkin RJ, Morris W, Adams C, Bourne B (2020) Petrophysics and mineral exploration: a workflow for data analysis and a new interpretation framework. Geophys Prospect 68:178–199. https://doi.org/10.1111/1365-2478.12882
36. Dentith M, Mudge S (2014) Geophysics for the mineral exploration geoscientist. AusIMM Bull. https://doi.org/10.1017/CBO9781139024358
37. Ding C, Peng H (2005) Minimum redundancy feature selection from microarray gene expression data. J Bioinform Comput Biol 3:185–205
38. Dufréchou G, Harris LB, Corriveau L, Antonoff V (2015) Regional and local controls on mineralization and pluton emplacement in the Bondy gneiss complex, Grenville Province, Canada interpreted from aeromagnetic and gravity data. J Appl Geophy 116:192–205. https://doi.org/10.1016/J.JAPPGEO.2015.03.015
39. Enayat M, Ghods A (2023) 3D Shear-Wave Velocity Model of Central Makran Using Ambient-Noise Adjoint Tomography. J Geophys Res Solid Earth 128. https://doi.org/10.1029/2023JB026928;PAGEGROUP:STRING:PUBLICATION e2023JB026928
40. Farahbakhsh E, Goel D, Pimparkar D, Muller RD, Chandra R (2025) Convolutional neural networks for mineral prospecting through alteration mapping with remote sensing data. https://doi.org/10.1007/s41064-025-00344-z
41. Farahnakian F, Sheikh J, Zelioli L, Nidhi D, Seppä I, Ilo R, Nevalainen P, Heikkonen J (2024) Addressing imbalanced data for machine learning based mineral prospectivity mapping. Ore Geol Rev 174:106270. https://doi.org/10.1016/J.OREGEOREV.2024.106270
42. Geranian H, Tabatabaei SH, Asadi HH, Carranza EJM (2016) Application of Discriminant Analysis and Support Vector Machine in Mapping Gold Potential Areas for Further Drilling in the Sari-Gunay Gold Deposit, NW Iran. Nat Resour Res 25:145–159. https://doi.org/10.1007/S11053-015-9271-2
43. Golmohammadi A, Karimpour MH, Shafaroudi AM, Mazaheri SA (2015) Alteration-mineralization, and radiometric ages of the source pluton at the Sangan iron skarn deposit, northeastern Iran. Ore Geol Rev 65:545–563
44. Ghorbani M (2013a) The economic geology of Iran: Mineral deposits and natural resources. The Economic Geology of Iran: Mineral Deposits and Natural Resources 1–569. https://doi.org/10.1007/978-94-007-5625-0
45. Ghorbani M (2013b) Metallogenic and mining provinces, belts and zones of Iran. Springer Geol 199–295. https://doi.org/10.1007/978-94-007-5625-0_6/FIGURES/26
46. Glennie KW, Hughes Clarke MW, Boeuf MGA, Pilaar WFH, Reinhardt BM (1990) Inter-relationship of Makran-Oman Mountains belts of convergence. Geological Society, London. https://doi.org/10.1144/GSL.SP.1992.049.01.47., Special Publications
47. Gonzalez-Alvarez I, Goncalves MA, Carranza EJM (2020) Introduction to the Special Issue Challenges for mineral exploration in the 21st century: Targeting mineral deposits under cover. Ore Geol Rev 126:103785. https://doi.org/10.1016/j.oregeorev.2020.103785
48. Groves DI, Santosh M, Müller D, Zhang L, Deng J, Yang LQ, Wang QF, Mineral systems: Their advantages in terms of developing holistic genetic models and for target generation in global mineral exploration. Geosystems and Geoenvironment 1., Bierlein DI (2022) F.P., 2007. Geodynamic settings of mineral deposit systems. J Geol Soc London 164, 19–30. https://doi.org/10.1144/0016-76492006-065

49. Guo P, Yang T (2023) Quantifying Continental Crust Thickness Using the Machine Learning Method. J Geophys Res Solid Earth 128:1–16. https://doi.org/10.1029/2022JB025970
50. Hajsadeghi S, Mirmohammadi M, Asghari O, Meshkani SA (2018) Geology and mineralization at the copper-rich volcanogenic massive sulfide deposit in Nohkouhi, Posht-e-Badam block, Central Iran. Ore Geol Rev 92:379–396. https://doi.org/10.1016/J.OREGEOREV.2017.11.030
51. Hassanlouei BT, Rajabzadeh MA (2019) Iron ore deposits associated with Hormuz evaporitic series in Hormuz and Pohl salt diapirs, Hormuzgan province, southern Iran. J Asian Earth Sci 172:30–55. https://doi.org/10.1016/j.jseaes.2018.08.024
52. Hassanpour S, Rajabpour S (2020) Magmatic-hydrothermal evolution of the Anjerd Cu skarn deposit, NW Iran: perspectives on mineral chemistry, fluid inclusions and stable isotopes. Ore Geol Rev 117:103269
53. He H, Zhu H, Yang X, Zhang W, Wang J (2024) Mineral prospectivity prediction based on convolutional neural network and ensemble learning. Scientific Reports 2024 14:1 14, 1–21. https://doi.org/10.1038/s41598-024-73357-0
54. Hezarkhani A (2006) Petrology of the intrusive rocks within the Sungun porphyry copper deposit, Azerbaijan, Iran. J Asian Earth Sci 27(3):326–340
55. Hezarkhani A (2008) Hydrothermal evolution of the Miduk Porphyry copper system, Kerman, Iran: A fluid inclusion investigation. Int Geol Rev 50:665–684. https://doi.org/10.2747/0020-6814.50.7.665
56. Holden EJ, Dentith M, Kovesi P (2008) Towards the automated analysis of regional aeromagnetic data to identify regions prospective for gold deposits. Comput Geosci 34:1505–1513. https://doi.org/10.1016/J.CAGEO.2007.08.007
57. Hronsky JMA, Groves DI (2008) Science of targeting: Definition, strategies, targeting and performance measurement. Aust J Earth Sci 55:3–12. https://doi.org/10.1080/08120090701581356;WGROUP:STRING:PUBLICATION
58. Irandoust MA, Priestley K, Sobouti F (2022) High-Resolution Lithospheric Structure of the Zagros Collision Zone and Iranian Plateau. J Geophys Res Solid Earth 127. https://doi.org/10.1029/2022JB025009
59. Jamali H, Mehrabi B (2015) Relationships between arc maturity and Cu-Mo-Au porphyry and related epithermal mineralization at the Cenozoic Arasbaran magmatic belt. Ore Geol Rev 65:487–501. https://doi.org/10.1016/J.OREGEOREV.2014.06.017
60. Kesler SE, Simon AC (2015) Mineral Resources, Economics and the Environment. https://doi.org/10.7302/22482
61. Kheyrollahi H, Alinia F, Ghods A (2018) Regional magnetic lithologies and structures as controls on porphyry copper deposits: Evidence from Iran. Explor Geophys 49:98–110. https://doi.org/10.1071/EG16042
62. Knox-Robinson CM, Wyborn LAI (1997) Towards a holistic exploration strategy: Using Geographic Information Systems as a tool to enhance exploration. Aust J Earth Sci 44:453–463. https://doi.org/10.1080/08120099708728326
63. Korehie MT, Ardebili O, Ahari HD, Shirzad MR, Fotovati V, Ghalamghash J, Kiani T, Najafi A, Soltani NS, Ashtiani ME, Farhatjah B (2019) Atlas of Iran's Geology and Mineral Distribution. Springer, Springer Nature
64. Leclerc F, Harris LB, Bédard JH, Van Breemen O, Goulet N (2012) Structural and stratigraphic controls on magmatic, volcanogenic, and shear zone-hosted mineralization in the Chapais-Chibougamau mining camp, northeastern Abitibi, Canada (1,2). Econ Geol 107:963–969. https://doi.org/10.2113/ECONGEO.107.5.963
65. Li Q, Chen G, Wang D (2024) Mineral Prospectivity Mapping Using Semi-supervised Machine Learning. https://doi.org/10.1007/S11004-024-10161-6/FIGURES/16. Math Geosci 1–31
66. Li S, Chen J, Liu C, Wang Y (2021) Mineral prospectivity prediction via convolutional neural networks based on geological big data. J Earth Sci 32:327–347. https://doi.org/10.1007/s12583-020-1365-z
67. Li YE, O'Malley D, Beroza G, Curtis A, Johnson P (2023) Machine Learning Developments and Applications in Solid-Earth Geosciences: Fad or Future? J Geophys Res Solid Earth 128. https://doi.org/10.1029/2022JB026310
68. Lösing M, Ebbing J (2021) Predicting Geothermal Heat Flow in Antarctica With a Machine Learning Approach. J Geophys Res Solid Earth 126:1–16. https://doi.org/10.1029/2020JB021499
69. Lou Y, Liu Y (2023) Mineral Prospectivity Mapping of Tungsten Polymetallic Deposits Using Machine Learning Algorithms and Comparison of Their Performance in the Gannan Region, China. Earth Space Sci 10. https://doi.org/10.1029/2022EA002596. e2022EA002596
70. Maepa F, Smith RS, Tessema A (2021) Support vector machine and artificial neural network modelling of orogenic gold prospectivity mapping in the Swayze greenstone belt, Ontario, Canada. Ore Geol Rev 130:103968. https://doi.org/10.1016/j.oregeorev.2020.103968

71. Maghfouri S, Hosseinzadeh MR (2018) The early Cretaceous Mansourabad shale-carbonate hosted Zn-Pb (-Ag) deposit, central Iran: An example of vent-proximal sub-seafloor replacement SEDEX mineralization. Ore Geol Rev 95:20–39
72. Maghfouri S, Rastad E, Momenzadeh M, Movahednia M, Hashempour SS, Jadehkenary KA, Ghaderi M, Konari MB, Izanloo J, Yarmohammadi A, Peernajmodin H (2025) Malayer-Esfahan Metallogenic Belt, Iran: Jurassic-Early Cretaceous sediment-(volcanic) hosted Zn-Pb (± Ba ± Ag), Fe-Mn-Pb (± Ba ± Cu) and Ba (± Pb ± Zn) deposits with evolution of basin. Journal of the Geological Society, jgs2024-284.
73. Mahboob MA, Celik T, Genc B (2024) Predictive modelling of mineral prospectivity using satellite remote sensing and machine learning algorithms. Remote Sens Appl 36:101316. https://doi.org/10.1016/J.RSASE.2024.101316
74. Mateus A, Martins L (2019) Challenges and opportunities for a successful mining industry in the future. Boletín Geológico y Min 130:99–121. https://doi.org/10.21701/BOLGEOMIN.130.1.007
75. McCuaig TC, Beresford S, Hronsky J (2010) Translating the mineral systems approach into an effective exploration targeting system. Ore Geol Rev 38:128–138. https://doi.org/10.1016/J.OREGEOREV.2010.05.008
76. McCuaig TC, Hronsky J (2017) The mineral systems concept: the key to exploration targeting. Appl Earth Sci 126:77–78. https://doi.org/10.1080/03717453.2017.1306274
77. McMillan M, Haber E, Peters B, Fohring J (2021) Mineral prospectivity mapping using a VNet convolutional neural network. Lead Edge 40:99–105. https://doi.org/10.1190/tle40020099.1
78. Mehrdar A, Motaghi K, Ghods A, Sobouti F, Priestley K, Pachhai S, Shabanian E, Zarunizadeh Z, Zeynaddini-Meymand R, El-Hussain I (2025) Crustal and uppermost mantle structure of the Iranian Makran subduction zone from ambient noise and earthquake surface wave tomography. Geophys J Int 241:70–85. https://doi.org/10.1093/GJI/GGAE419
79. Meshkani SA, Mehrabi B, Yaghubpur A, Sadeghi M (2013) Recognition of the regional lineaments of Iran: Using geospatial data and their implications for exploration of metallic ore deposits. Ore Geol Rev 55:48–63. https://doi.org/10.1016/J.OREGEOREV.2013.04.007
80. Mehrabi B, Siani MG, Goldfarb R, Azizi H, Ganerod M, Marsh EE (2016) Mineral assemblages, fluid evolution, and genesis of polymetallic epithermal veins, Glojeh district, NW Iran. Ore Geol Rev 78:41–57
81. Mollai H, Sharma R, Pe-Piper G (2009) Copper mineralization around the Ahar batholith, north of Ahar (NW Iran): Evidence for fluid evolution and the origin of the skarn ore deposit. Ore Geol Rev 35:401–414. https://doi.org/10.1016/j.oregeorev.2009.02.005
82. Monsef I, Monsef R, Mata J, Zhang Z, Pirouz M, Rezaeian M, Esmaeili R, Xiao W (2018) Evidence for an early-MORB to fore-arc evolution within the Zagros suture zone: Constraints from zircon U-Pb geochronology and geochemistry of the Neyriz ophiolite (South Iran). Gondwana Res 62:287–305. https://doi.org/10.1016/J.GR.2018.03.002
83. Monsef I, Rahgoshay M, Pirouz M, Chiaradia M, Grégoire M, Ceuleneer G (2019) The Eastern Makran Ophiolite (SE Iran): evidence for a Late Cretaceous fore-arc oceanic crust. Int Geol Rev 61:1313–1339. https://doi.org/10.1080/00206814.2018.1507764
84. Monsef I, Zhang Z, Shabanian E, le Roux P, Rahgoshay M (2022) Tethyan subduction and Cretaceous rift magmatism at the southern margin of Eurasia: Evidence for crustal evolution of the South Caspian Basin. Earth Sci Rev 228:104012. https://doi.org/10.1016/J.EARSCIREV.2022.104012
85. Moritz R, Ghazban F, Singer BS (2006) Eocene gold ore formation at Muteh, Sanandaj-Sirjan tectonic zone, western Iran: A result of late-stage extension and exhumation of metamorphic basement rocks within the Zagros orogen. Econ Geol 101:1497–1524. https://doi.org/10.2113/GSECONGEO.101.8.1497
86. Mousivand F, Rastad E, Peter JM, Maghfouri S (2018) Metallogeny of volcanogenic massive sulfide deposits of Iran. Ore Geol Rev 95:974–1007
87. Nabatian G, Rastad E, Neubauer F, Honarmand M, Ghaderi M (2015) Iron and Fe–Mn mineralisation in Iran: implications for Tethyan metallogeny. Aust J Earth Sci 62:211–241. https://doi.org/10.1080/08120099.2015.1002001
88. Omidianfar S, Monsef I, Rahgoshay M, Zheng J, Cousens B (2020) The middle Eocene high-K magmatism in Eastern Iran Magmatic Belt: constraints from U-Pb zircon geochronology and Sr-Nd isotopic ratios. Int Geol Rev 62:1751–1768. https://doi.org/10.1080/00206814.2020.1716272
89. Parsa M, Carranza EJM (2021) Modulating the impacts of stochastic uncertainties linked to deposit locations in data-driven predictive mapping of mineral prospectivity. Nat Resour Res 30:3081–3097. https://doi.org/10.1007/s11053-021-09891-9

90. Parsa M, Maghsoudi A (2021) Assessing the effects of mineral systems-derived exploration targeting criteria for random Forests-based predictive mapping of mineral prospectivity in Ahar-Arasbaran area, Iran. Ore Geol Rev 138:104399. https://doi.org/10.1016/j.oregeorev.2021.104399
91. Pavlis NK, Holmes SA, Kenyon SC, Factor JK (2012a) The development and evaluation of the Earth Gravitational Model 2008 (EGM2008). J Geophys Res Solid Earth 117:1–38. https://doi.org/10.1029/2011JB008916
92. Pavlis NK, Holmes SA, Kenyon SC, Factor JK (2012b) The development and evaluation of the Earth Gravitational Model 2008 (EGM2008). J Geophys Res Solid Earth 117:1–38. https://doi.org/10.1029/2011JB008916
93. Penney C, Tavakoli F, Saadat A, Nankali HR, Sedighi M, Khorrami F, Sobouti F, Rafi Z, Copley A, Jackson J, Priestley K (2017) Megathrust and accretionary wedge properties and behaviour in the Makran subduction zone. Geophys J Int 209:1800–1830. https://doi.org/10.1093/gji/ggx126
94. Petrella L, Williams-Jones AE, Goutier J, Walsh J (2014) The nature and origin of the rare earth element mineralization in the misery syenitic intrusion, Northern Quebec, Canada. Econ Geol 109:1643–1666. https://doi.org/10.2113/ECONGEO.109.6.1643
95. Qaderi S, Maghsoudi A, Pour AB, Yousefi M (2024) Geological Controlling Factors on Mississippi Valley-Type Pb-Zn Mineralization in Western Semnan, Iran. Minerals (2075-163X), 14(9).
96. Rajabi A, Rastad E, Canet C (2013) Metallogeny of Permian-Triassic carbonate-hosted Zn-Pb and F deposits of Iran: A review for future mineral exploration. Aust J Earth Sci 60(2):197–216
97. Richards JP (2015) Tectonic, magmatic, and metallogenic evolution of the Tethyan orogen: From subduction to collision. Ore Geol Rev 70:323–345. https://doi.org/10.1016/J.OREGEOREV.2014.11.009
98. Richards JP, Wilkinson D, Ullrich T (2006) Geology of the Sari Gunay epithermal gold deposit, northwest Iran. Econ Geol 101:1455–1496. https://doi.org/10.2113/GSECONGEO.101.8.1455
99. Rodriguez-Galiano V, Sanchez-Castillo M, Chica-Olmo M, Chica-Rivas M, Machine learning predictive models for mineral prospectivity: An evaluation of neural networks, random forest, regression trees and support vector machines. Ore Geol Rev 71, 804–818., Sahandi M, Soheili M (2015) 2014. Geological Map of Iran, scale 1:1000000. Geological Survey of Iran
100. Shahabpour J (1999) The role of deep structures in the distribution of some major ore deposits in Iran, NE of the Zagros thrust zone. J Geodyn 28:237–250. https://doi.org/10.1016/S0264-3707(98)00040-4
101. Shayeganpour S, Tangestani MH (2022) Extraction of rock and alteration geons by FODPSO segmentation and GP regression on the HyMap imagery: A case study of SW Birjand, Eastern Iran. Ore Geol Rev 143:104767. https://doi.org/10.1016/J.OREGEOREV.2022.104767
102. Shirmard H, Farahbakhsh E, Müller RD, Chandra R (2022) A review of machine learning in processing remote sensing data for mineral exploration. Remote Sens Environ 268. https://doi.org/10.1016/j.rse.2021.112750
103. Singer DA (2007) Estimating amounts of undiscovered mineral resources. In Proceedings for a Workshop on Deposit Modeling, Mineral Resource Assessment, and Their Role in Sustainable Development: USGS Circular. (Vol. 1294, pp. 79–84)
104. Soloviev SG, Kryazhev SG, Dvurechenskaya SS, Vasyukov VE, Shumilin DA, Voskresensky KI (2019) The superlarge Malmyzh porphyry Cu-Au deposit, Sikhote-Alin, eastern Russia: Igneous geochemistry, hydrothermal alteration, mineralization, and fluid inclusion characteristics. Ore Geol Rev 113. https://doi.org/10.1016/j.oregeorev.2019.103112
105. Stampfli GM (2000) Tethyan oceans. Geological Society, London, Special Publications 173, 1–23. https://doi.org/10.1144/GSL.SP.2000.173.01.01
106. Stampfli GM, Borel GD (2004) The TRANSMED Transects in Space and Time: Constraints on the Paleotectonic Evolution of the Mediterranean Domain. Springe, Berlin, pp 53–90
107. Stampfli GM, Borel GD (2002) A plate tectonic model for the Paleozoic and Mesozoic constrained by dynamic plate boundaries and restored synthetic oceanic isochrons. Earth Planet Sci Lett 196:17–33. https://doi.org/10.1016/S0012-821X(01)00588-X
108. Stöcklin J (1974) Possible Ancient Continental Margins in Iran. The Geology of Continental Margins. Springer, Berlin Heidelberg, pp 873–887. https://doi.org/10.1007/978-3-662-01141-6_64
109. Stocklin J (1968) Structural History and Tectonics of Iran: A Review. Am Assoc Pet Geol Bull 52:1229–1258
110. Stöcklin J (1968) Structural history and tectonics of Iran: a review. Am Assoc Pet Geol Bull 52:1229–1258
111. Stosch HG, Romer RL, Daliran F, Rhede D (2011) Uranium-lead ages of apatite from iron oxide ores of the Bafq District, East-Central Iran. Min Depos 46:9–21. https://doi.org/10.1007/S00126-010-0309-4

112. Sun T, Li H, Wu K, Chen F, Zhu Z, Hu Z (2020) Data-driven predictive modelling of mineral prospectivity using machine learning and deep learning methods: a case study from southern Jiangxi Province China. Minerals 10:102. https://doi.org/10.3390/min10020102
113. Tagwai MG, Jimoh OA, Shehu SA, Zabidi H (2024) Application of GIS and remote sensing in mineral exploration: current and future perspectives. World J Eng 21:487–502. https://doi.org/10.1108/WJE-09-2022-0395
114. TaleFazel E, Mehrabi B, GhasemiSiani M (2019) Epithermal systems of the Torud-Chah Shirin district, northern Iran: Ore-fluid evolution and geodynamic setting. Ore Geol Rev 109:253–275
115. Teknik V (2024) The improved Moho depth imaging in the Arabia-Eurasia collision zone: A machine learning approach integrating seismic observations and satellite gravity data. Tectonophysics 893:230553. https://doi.org/10.1016/j.tecto.2024.230553
116. Teknik V, Artemieva IM, Thybo H (2024) Limited arc magmatism and seismicity due to extensive mantle wedge serpentinization in the Makran subduction zone. Earth Planet Sci Lett 645:118950. https://doi.org/10.1016/j.epsl.2024.118950
117. Teknik V, Ghods A (2017) Depth of magnetic basement in Iran based on fractal spectral analysis of aeromagnetic data. Geophys J Int 209:1878–1891. https://doi.org/10.1093/gji/ggx132
118. Teknik V, Thybo H, Artemieva IM, Ghods A (2020) A new tectonic map of the Iranian plateau based on aeromagnetic identification of magmatic arcs and ophiolite belts. Tectonophysics 792. https://doi.org/10.1016/J.TECTO.2020.228588
119. Torab FM, Lehmann B (2007) Magnetite-apatite deposits of the Bafq district, Central Iran: apatite geochemistry and monazite geochronology. Mineral Mag 71:347–363. https://doi.org/10.1180/MINMAG.2007.071.3.347
120. Verdel C, Wernicke BP, Hassanzadeh J, Guest B (2011) A Paleogene extensional arc flare - up in Iran. Tectonics 30:1–20. https://doi.org/10.1029/2010TC002809
121. Wake N, Farahbakhsh E, Müller RD (2024) Lateritic Ni–Co Prospectivity Modeling in Eastern Australia Using an Enhanced Generative Adversarial Network and Positive-Unlabeled Bagging. https://doi.org/10.1007/S11053-024-10423-4. Natural Resources Research
122. Woodhead J, Landry M (2021) Harnessing the Power of Artificial Intelligence and Machine Learning in Mineral Exploration—Opportunities and Cautionary Notes. SEG Discovery 19–31. https://doi.org/10.5382/Geo-and-Mining-13
123. Xiong Y, Zuo R (2020) Recognizing multivariate geochemical anomalies for mineral exploration by combining deep learning and one-class support vector machine. Comput Geosci 140. https://doi.org/10.1016/j.cageo.2020.104484
124. Xiong Y, Zuo R (2018) GIS-based rare events logistic regression for mineral prospectivity mapping. Comput Geosci 111:18–25. https://doi.org/10.1016/j.cageo.2017.10.005
125. Xiong Y, Zuo R, Carranza EJM (2018) Mapping mineral prospectivity through big data analytics and a deep learning algorithm. Ore Geol Rev 102:811–817. https://doi.org/10.1016/j.oregeorev.2018.10.006
126. Yang H, huan, Wang Q, Li Ybo, Lin B, Song Y, Wang Y, yun, He W, Li H, wei, Li S, Li J, li, Liu C, cheng, Feng S, bin, Xin T, Fu Xlian, Liang X, juan, Zhang Q, Wang Bqi, Li Y (2022) Geology and mineralization of the Tiegelongnan supergiant porphyry-epithermal Cu (Au, Ag) deposit (10 Mt) in western Tibet, China: A review. China Geol 5:136–159. https://doi.org/10.1016/S2096-5192(22)00091-X
127. Yang N, Zhang Z, Yang J, Hong Z (2022) Mineral prospectivity prediction by integration of convolutional autoencoder network and random forest. Nat Resour Res 31:1103–1119. https://doi.org/10.1007/s11053-022-10038-7
128. Yin B, Zuo R, Sun S (2023) Mineral prospectivity mapping using deep self-attention model. Nat Resour Res 32:37–56. https://doi.org/10.1007/s11053-022-10142-8
129. Yin J, Li N (2022) Ensemble learning models with a Bayesian optimization algorithm for mineral prospectivity mapping. Ore Geol Rev 145. https://doi.org/10.1016/j.oregeorev.2022.104916
130. Zarasvandi A, Liaghat S, Zentilli M (2005) Geology of the Darreh-Zerreshk and Ali-Abad porphyry copper deposits, central Iran. Int Geol Rev 47(6):620–646
131. Zarasvandi A, Liaghat S, Zentilli M, Reynolds PH (2007) 40Ar/39Ar geochronology of alteration and petrogenesis of porphyry copper-related granitoids in the Darreh-Zerreshk and Ali-Abad area, central Iran. Explor Min Geol 16:11–24. https://doi.org/10.2113/GSEMG.16.1-2.11

132. Zarasvandi A, Rezaei M, Sadeghi M, Lentz D, Adelpour M, Pourkaseb H (2015) Rare earth element signatures of economic and sub-economic porphyry copper systems in Urumieh-Dokhtar Magmatic Arc (UDMA), Iran. Ore Geol Rev 70:407–423. https://doi.org/10.1016/J.OREGEOREV.2015.01.010
133. Zarasvandi A, Rezaei M, Raith JG, Asadi S, Lentz D (2019) Hydrothermal fluid evolution in collisional Miocene porphyry copper deposits in Iran: Insights into factors controlling metal fertility. Ore Geol Rev 105:183–200
134. Zhang SE, Lawley CJM, Bourdeau JE, Nwaila GT, Ghorbani Y (2024) Nat Resour Res 2024 33(3 33):995–1023. https://doi.org/10.1007/S11053-024-10322-8. Workflow-Induced Uncertainty in Data-Driven Mineral Prospectivity Mapping
135. Zhao P (2007) Quantitative mineral prediction and deep mineral exploration. Earth Sci Front 14:1–10
136. Zuo R, Xu Y (2023) Graph deep learning model for mapping mineral prospectivity. Math Geosci 55:1–21. https://doi.org/10.1007/s11004-022-10015-z
137. Zuo R, Peng Y, Li T, Xiong Y (2021) Challenges of geological prospecting big data mining and integration using deep learning algorithms. Earth Sci 46:350–358

Figures

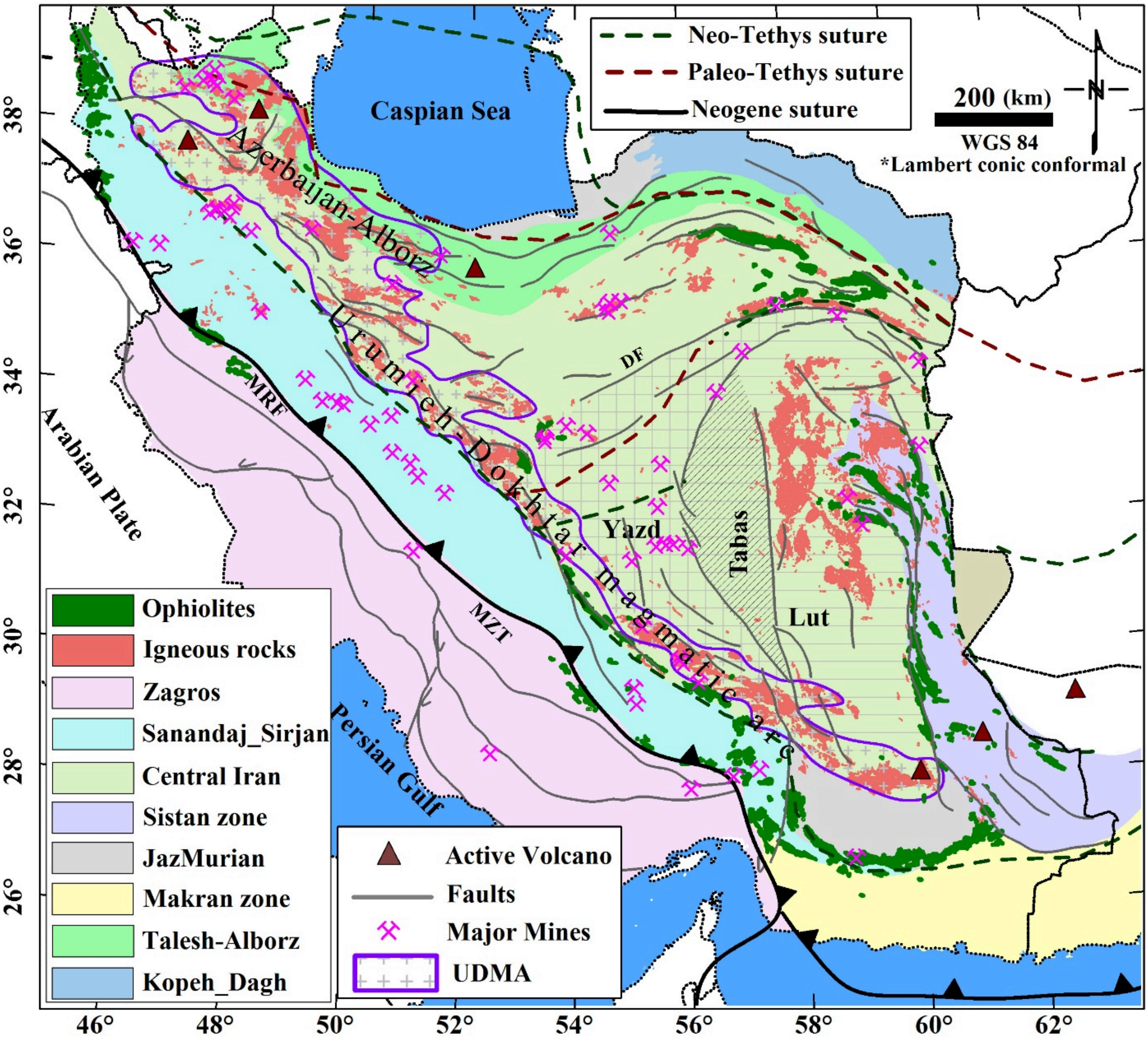

Figure 1

Simplified Tectono-magmatic map of the Iranian plateau (modified after Sahandi and Soheili, 2014) overlaid by the location of the major Fe, Cu, Pb, Zn, and Au ore deposits (see Table 1; after Meshkani et al., 2013). Abbreviations: DF, Dorouneh Fault; MRF, Main Recent Fault; MZT, Main Zagros Thrust; UDMA, Urumieh-Dokhtar magmatic arc. The Zagros suture zone lies approximately along MRF and MZT.

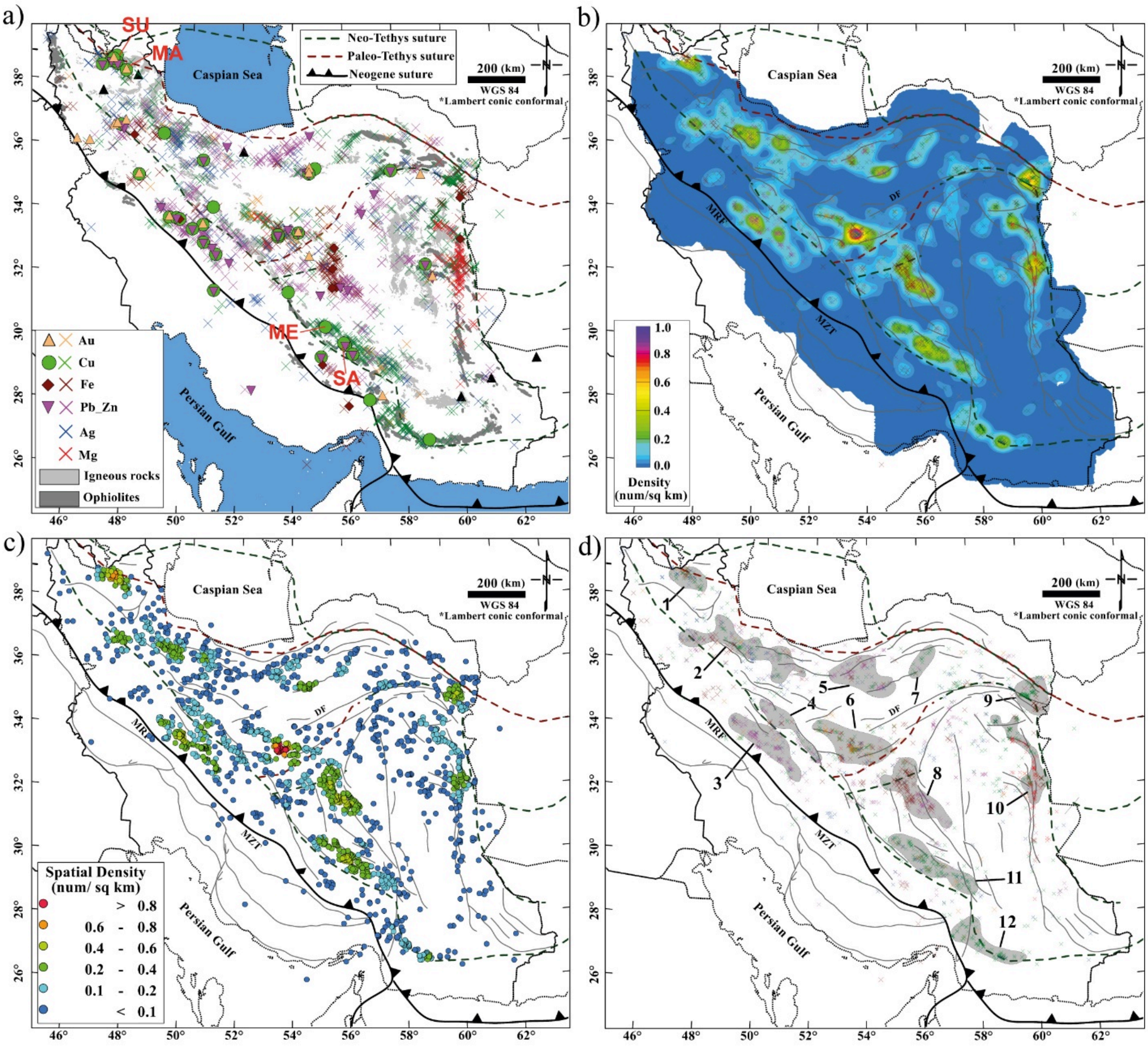

Figure 2

a) Distribution map of the seven ore deposits (Cu, Fe, Au, Pb-Zn, Ag, and Mg). The crosses indicate the location of the mineral deposits without detailed information on their grade and size of the deposits (Korehie et al., 2019). This dataset includes 2037 observation points used for training and validation with 5-fold cross-validation. The black triangles represent quaternary volcanic cones. The symbols other than crosses and black triangles are major known deposits (see Table 1; after Meshkani et al., 2013), which are used for testing. The colour of the symbols indicates the type of mineral. Abbreviations: SA, Sarcheshmeh copper deposit; ME, Meiduk copper deposit; MA, Mazraeh copper deposit; SU, Sungon copper deposits **b**) The spatial density of the mineral occurrence with no detailed information. The pale crosses indicate the location of mineral deposits. **c**) The resampled spatial density of the mineral deposits at their corresponding locations. **d**) Metallogenic zones modified after Ghorbani (2013)and updated based on the high spatial density (> 0.2 num/sq km) of mineral deposits. The numbers correspond to the metallogenic zone names as follows: (1) KaraDagh; (2) Takab-Tarom-Hashtjin; (3) Malayer-Isfahan; (4) Kashan-Natanz; (5) Toroud; (6) Anarak; (7) QaleBala; (8) Bafgh; (9) Khaf; (10) Nehbandan-Ferdous; (11) Jiroft-Shahrebabak; (12) Kahnuj-Fanuj.

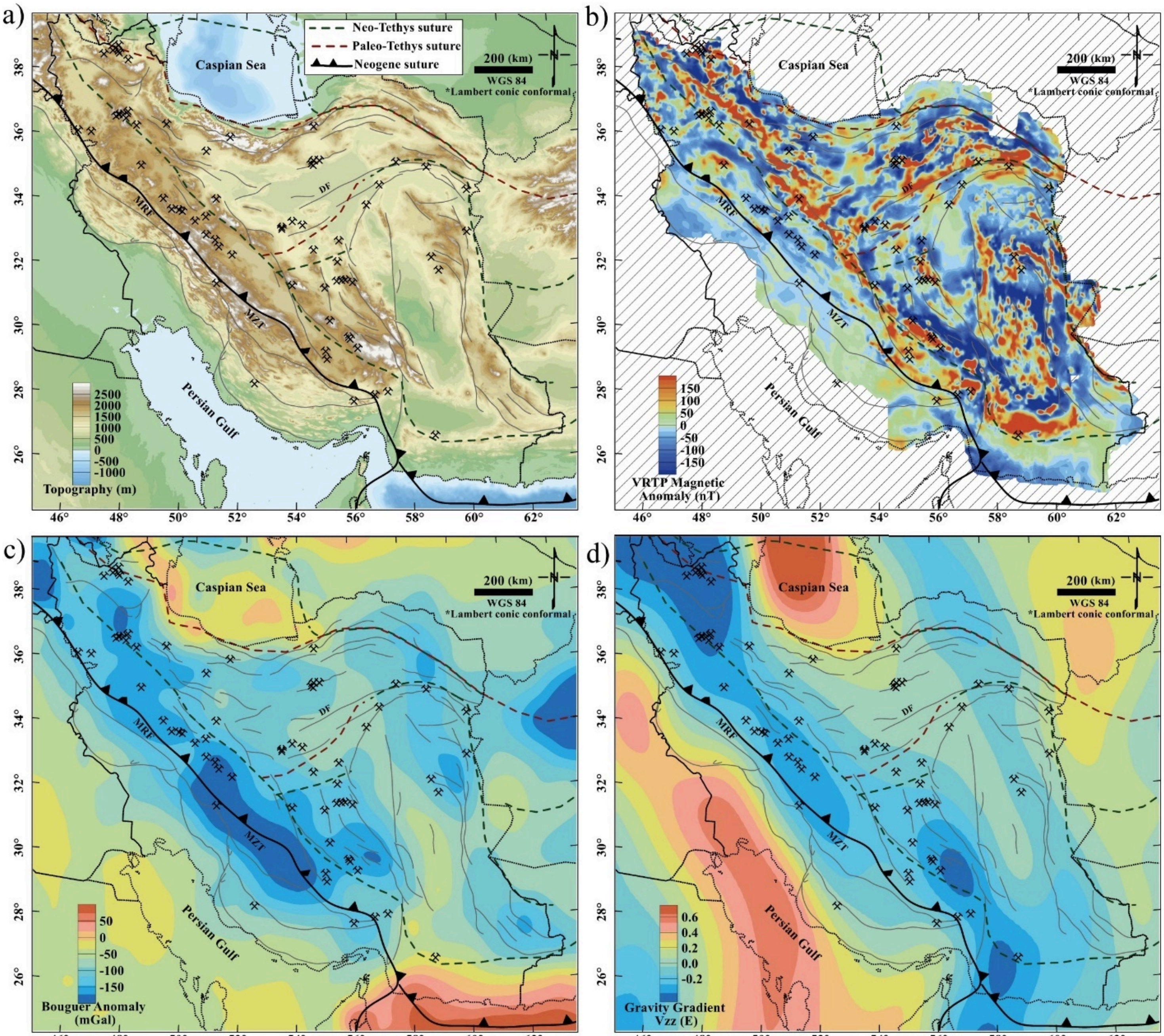

Figure 3

Selected geophysical training measurements, including **a**) digital elevation model from the ETOPO1 global elevation model (Amante and Eakins, 2009). The symbols indicated major known ore deposits (Table 1), which are grouped for quality checking of the final AI-model; **b**) the variable reduced-to-pole (VRTP) total magnetic intensity (TMI) (Teknik and Ghods, 2017). **c**) The Bouguer anomaly map derived by a compilation of terrestrial, altimetry-derived, and airborne gravity measurements, as incorporated in the EGM2008 global Bouguer anomaly model (Pavlis et al., 2012); and **d**) The vertical Vzz component of gravity gradients at 225 km above the Earth's surface with respect to WGS84 (Bouman et al., 2016). To make the vertical derivative map (panel d), the Z-axis is considered to point up.

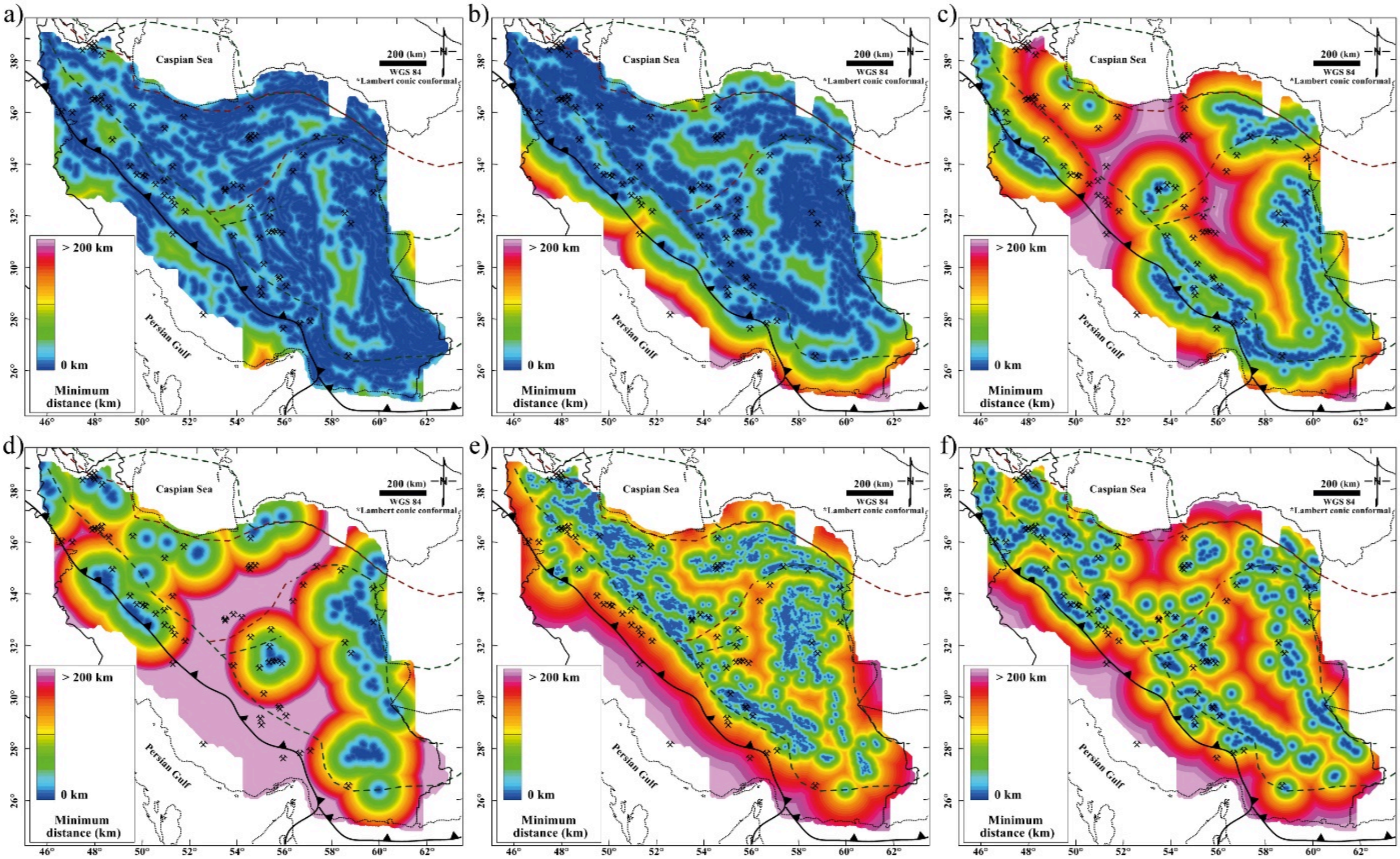

Figure 4

The selected features of the calculated minimum distance to **a**) the faults (Sahandi and Soheili, 2014); **b**) the igneous outcrops; **c**) the ophiolite outcrops; **d**) the andesite outcrops; **e**) the Eocene igneous outcrops; and **f**) the granite outcrops.

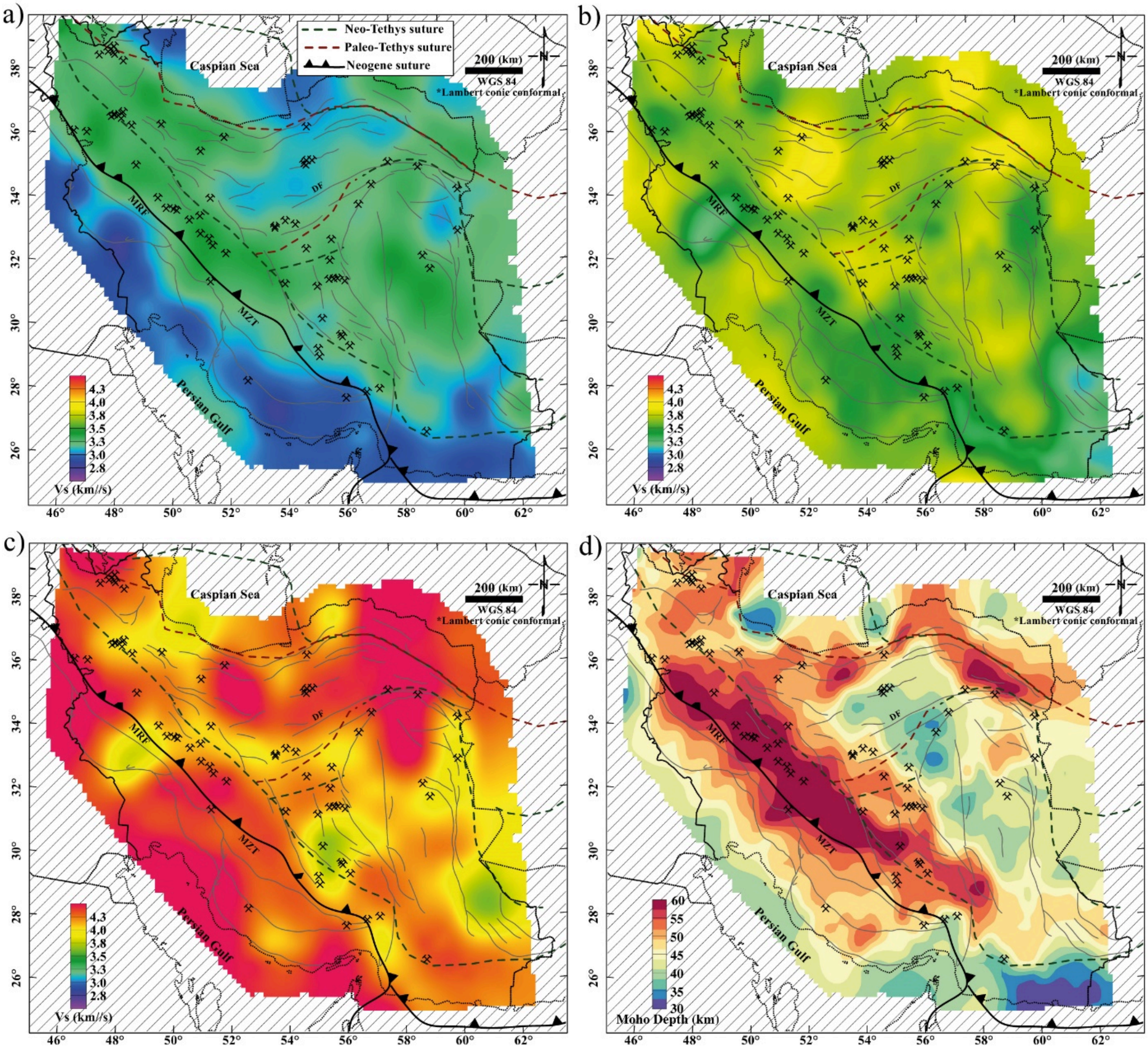

Figure 5

Lithosphere structure training features (Irandoust et al., 2022) are **a**) averaged upper crustal shear velocity; **b**) averaged lower crustal shear velocity; **c**) averaged upper mantle shear velocity; and **d**) Moho depth.

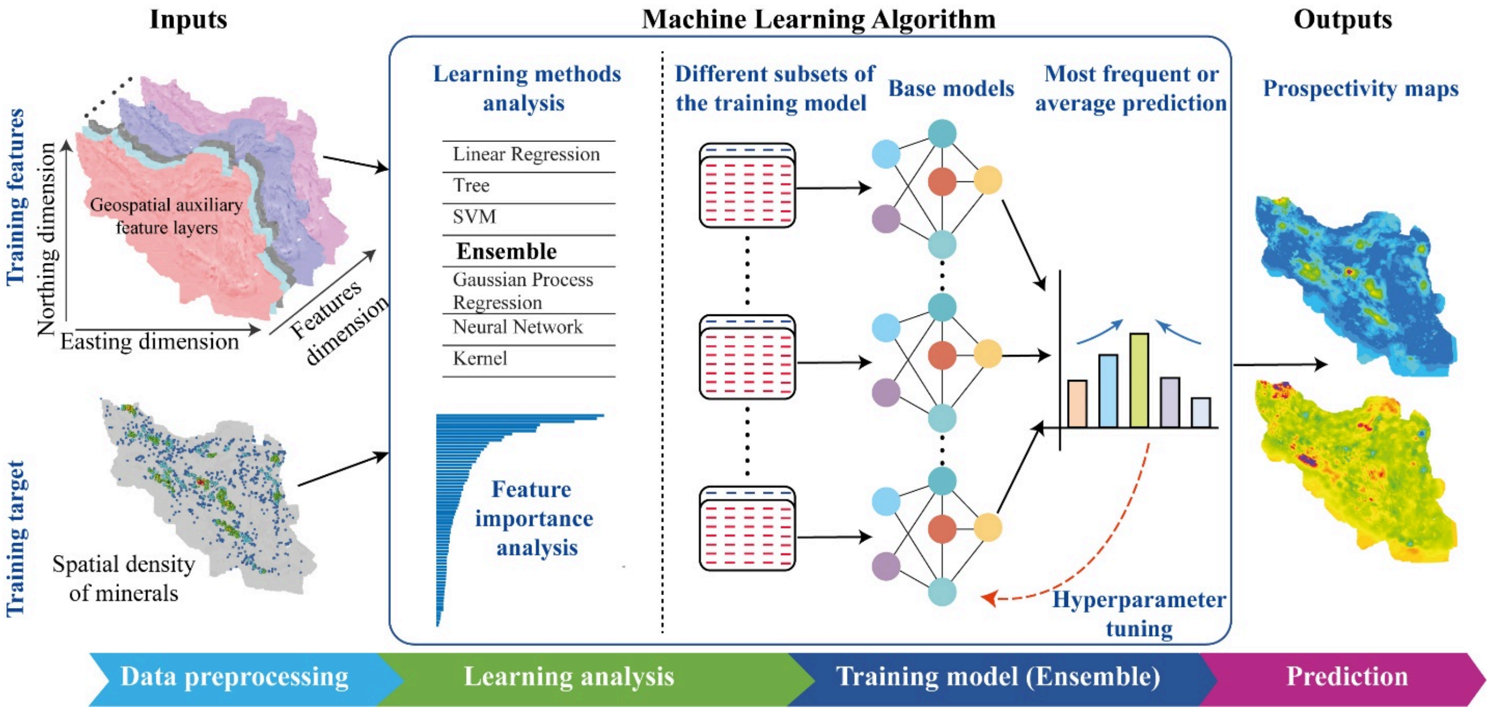

Figure 6

Simplified workflow of Mineral Prospectivity Mapping (MPM) approach. The process flows from left to right, beginning with the preparation and pre-processing of geospatial auxiliary feature layers (training features) and calculation of spatial density of known ore deposits (training target). Learning methods are evaluated to identify suitable algorithms (e.g., Linear Regression, SVM, Ensemble and Neural Networks). Feature importance is analyzed. Ensemble Bagged Trees with Neural Networks base models are selected due to their optimum performance. Hyperparameter tuning is applied to achieve optimize performance. Predictions from multiple base models are aggregated (e.g., via averaging or majority voting) to produce final mineral prospectivity maps highlighting zones with high mineral potential.

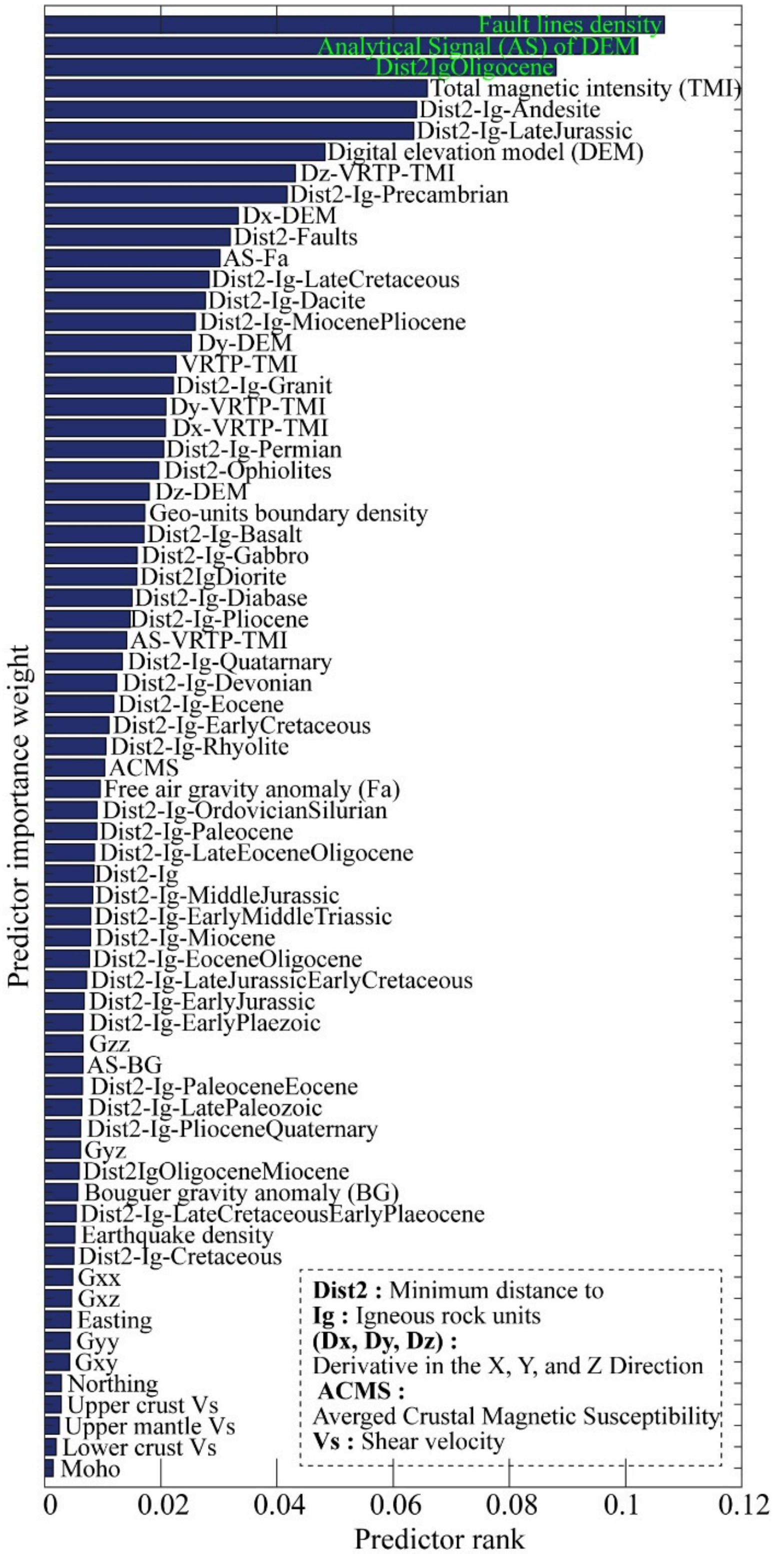

Figure 7

The importance of the training features determined by the Minimum Redundancy and Maximum Relevance (MRMR) algorithm (Ding and Peng, 2005).

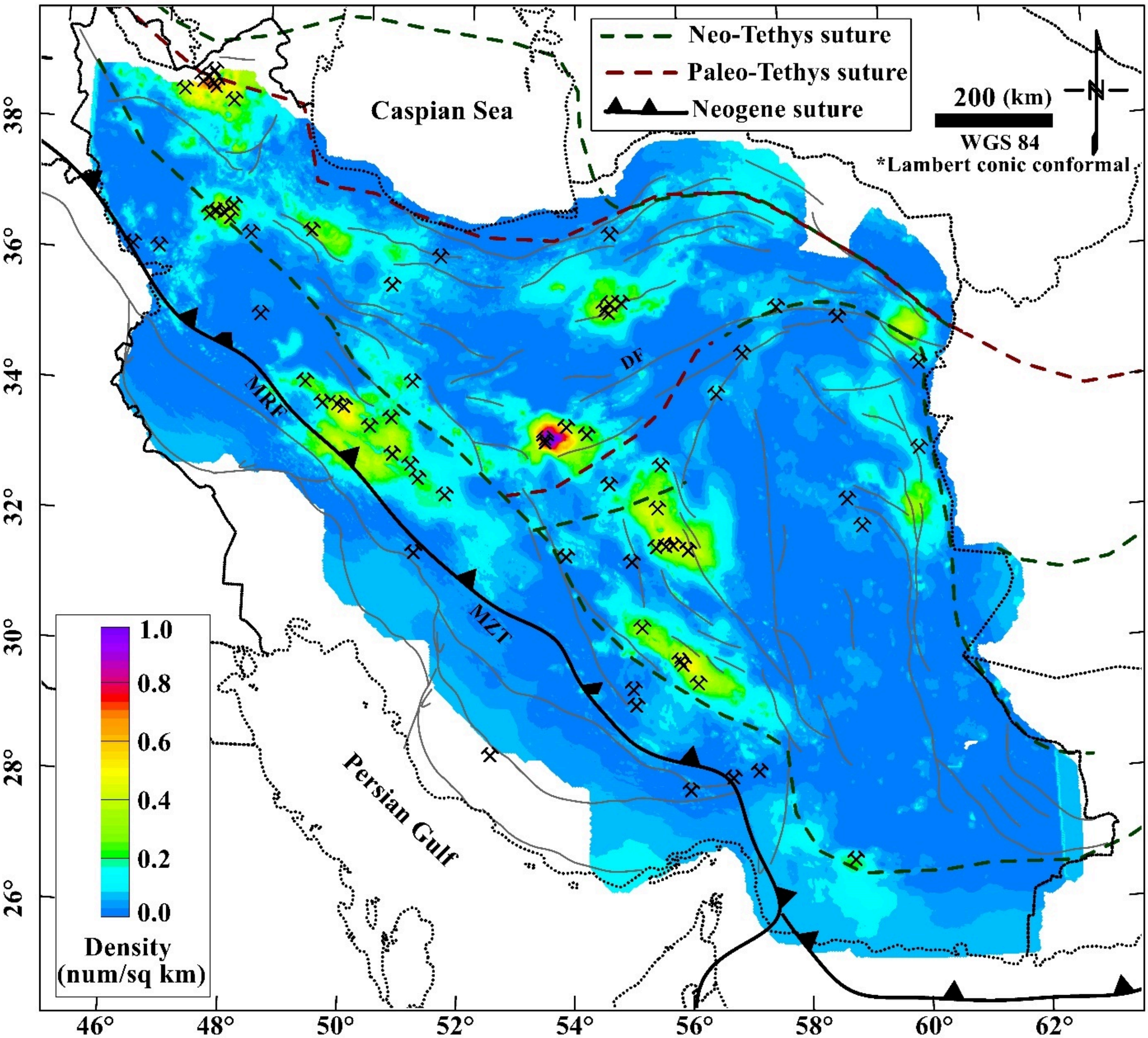

Figure 8

The predicted spatial density of the ore deposits (i.e., metallogenic intensity) across the Iranian plateau, achieved by the Ensemble Bagged Trees method.

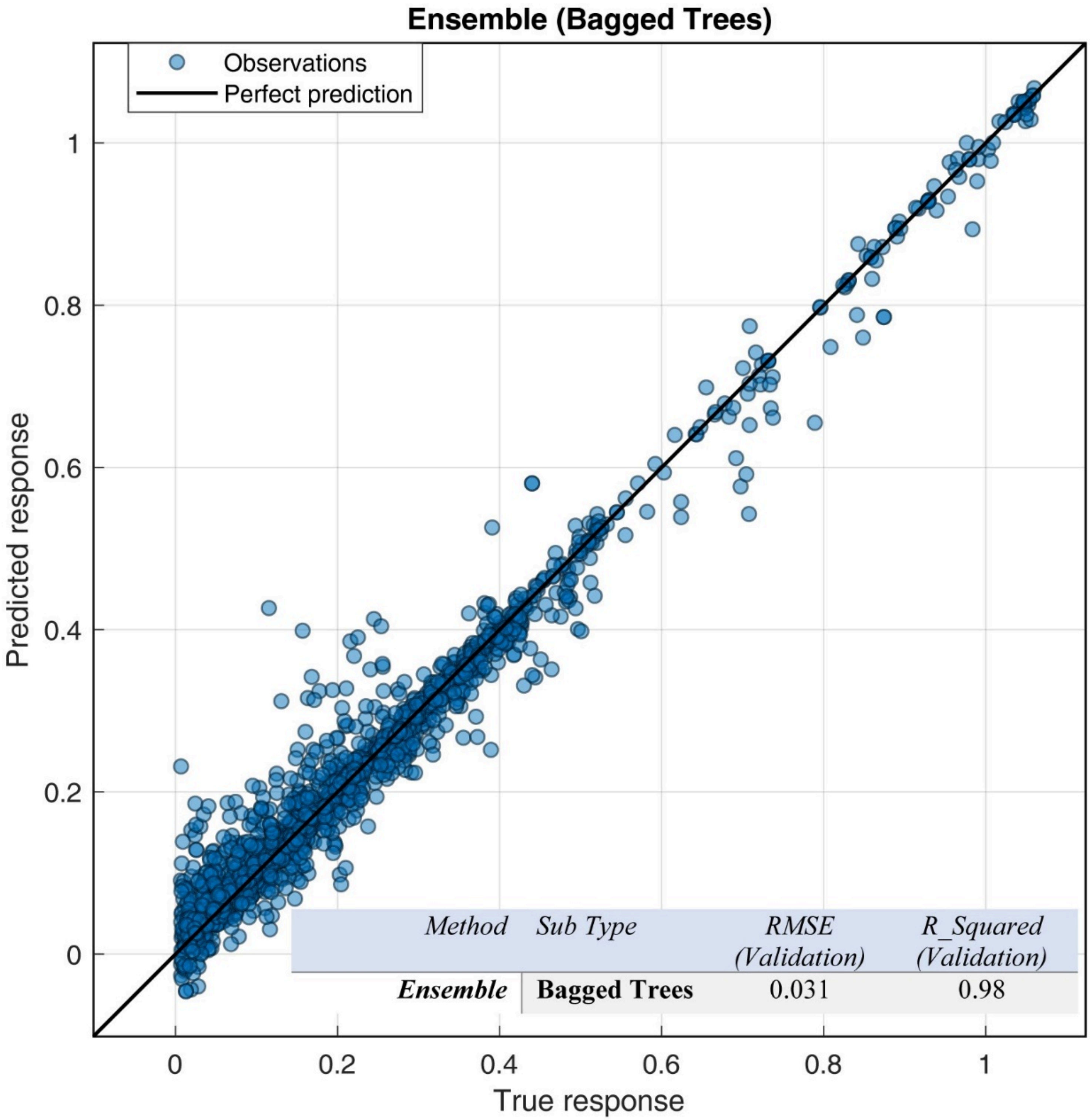

Figure 9

The scatter plot compares the predicted spatial density of mineral deposits with the observation (Figure 2b). The prediction model was computed by the Ensemble Bagged Trees method, showing a high coefficient of correlation (R^2) of 0.98.

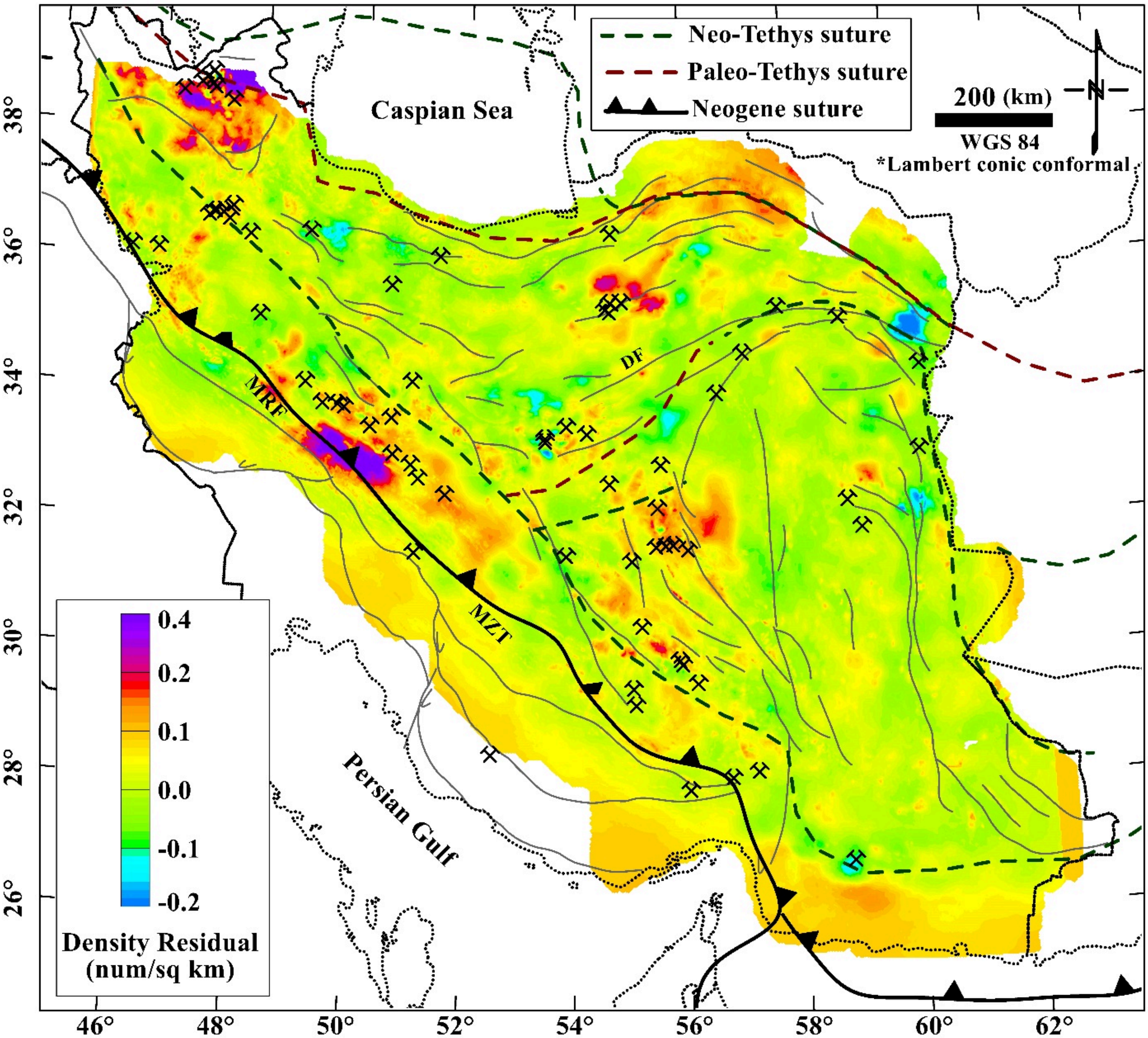

Figure 10

The residual density of the ore deposits (i.e., residual metallogenic intensity) derived by subtracting the predicted spatial density of the ore occurrence (Figure 8) from the observed spatial density of the ore occurrence (Figure 2b).

Supplementary Files

This is a list of supplementary files associated with this preprint. Click to download.

- Supplementary.docx